UC Riverside
UC Riverside Electronic Theses and Dissertations

Title
Prospects of Two-Dimensional Devices: Electrical and Optical Characterization of Transition Metal Dichalcogenide Films

Permalink
https://escholarship.org/uc/item/15n9k8m5

Author
Klee, Velveth

Publication Date
2016

Peer reviewed|Thesis/dissertation

eScholarship.org Powered by the California Digital Library
University of California

UNIVERSITY OF CALIFORNIA
RIVERSIDE

Prospects of Two-Dimensional Devices: Electrical and Optical Characterization of Transition Metal Dichalcogenide Films

A Dissertation submitted in partial satisfaction
of the requirements for the degree of

Doctor of Philosophy

in

Materials Science and Engineering

by

Velveth Klee

December 2016

Dissertation Committee:
Dr. Ludwig Bartels, Chairperson
Dr. De-en Jiang
Dr. Joshua C. H. Lui

Copyright by
Velveth Klee
2016

The Dissertation of Velveth Klee is approved:

____

____

____

Committee Chairperson

University of California, Riverside

ACKNOWLEDGEMENTS

I would like to thank my principal investigator and advisor, Professor Ludwig Bartels, for giving me the opportunity to work in his lab and for guiding me throughout these last four years. I especially want to thank him for the many challenges he presented me with. Overcoming these challenges has given me confidence, determination, and work ethic that will continue to propel me as a researcher and educator. Lastly, I would like to thank Professor Bartels for giving me the opportunity to work on projects where I had the chance to work in national labs, travel to national conferences, and collaborate with industry partners.

I would like to thank the following professors for serving on my advancement and doctoral committees: Je-en Jiang, Joshua C. H. Lui, Marc Bockrath, Yadong Yin, Roger Lake, and David Bocian. I thank you for your time and effort spent working with me during these exams, especially under such short notice.

A major part of this work was completed at Sandia National Labs. I would like to thank Francois and Alec for their mentoring and scientific training while I worked with them at Sandia. My time spent at Sandia was full of growth and many challenging, yet rewarding experiences. I gained so much knowledge while at Sandia and am incredibly grateful to have had the opportunity to work with such brilliant and kind scientists, as Francois and Alec. In particular, I would like to than Francois and his wife, Marie, for allowing me to live with them during my long visit. While living with them, I was exposed to a whole new lifestyle of health, learning, and responsibility that I still carry

with me. I am truly fortunate to have met them and I know that my success at Sandia would not have happened without their support.

During my time in the Bartels group, our lab grew from 8 graduate students to nearly 20 graduate students and 30 undergraduates. I am very lucky and grateful to have met so many hard working, determined, and intelligent individuals and I thank each of you for adding to my doctoral work. I would especially like to thank the following people: John, Sarah, Quan, Yeming, Chen, Wenhao, Jon W., KatieMarie, Greg, Dezheng, Mark, Ariana, Edwin, Sahar, Tammy, David, Tom, Joe, Mike, I-Hsi, Cindy, Koichi, Miguel, Adam, Michelle, Aimee, Alison, Eva, Ariana N., Miguel, and Brandon. I truly feel like you were all a part of my family and I thank you for your friendship and kindness you have showed me. There are no words to express how grateful I am to have you all in my life. I appreciate every bit of help you all have given me.

Completing this doctoral program would not have been possible without a very large community of support. From near and far I have been blessed with many wonderful people that always believed in my dreams. I would like to thank my mom, brother, grandfather, aunt and cousins in Denver for supporting me and allowing me the opportunity to work and study towards completing my degree. I would like to thank my dad, Bere, Lindsay, Jayson, Ruben, Manuel, Isaias, Myriam, Will, William, Joanne, and family in Chicago and Guatemala for their continuous support, advice, and well-wishes for completing my studies. I would like to thank Marco, Estela, Marisa, AD, Spencer, Maria Estela, Rita, Sergio, Marco Sr., Lucas, Lulu, and Charlie, my adopted family, for their unwavering support and, especially, to the women of this family for showing me

how to be a strong and independent woman. To all my family: there were many times that I was late or completely missed events, and many more times that I was so tired from working that I would just fall asleep any time I visited. You all understood and accepted my situation. Throughout these last four years, your support was the driving force that kept me going. I knew that you would love and support me whether I finished this program or not; however, the incredible belief each of you had in my abilities as a scientist and student gave me the strength to believe in myself and finish this program even when I was certain I couldn't come up with a solution to a frustrating problem (a new approach was all I needed).

I would like to thank my friends for always reminding me of my talents. I have known for a long time that I liked science and wanted to do something where I would continuously be a learner. There were many times when I had doubt and felt like an imposter in the university. My friends were especially helpful in reminding me of all my accomplishments and the many obstacles I have overcome. In particular, my friends hold me to a standard of excellence that I strive to achieve. I would like to thank the following friends (in particular all the badass women): Jhenzier, Gail, Juan, Sonya, Yadhira, Marisa, AD, Estela, Emil, Carlos, Henry, Ja'Dell, Katrina, Matt, Claudia, Judith, Nicholas D., Stephanie, David G., Raul, Min, Erika, Darren, Devin, Alejandra, Dejeunee, Jonathan, Godfrey, and Melissa (and the Jensen family).

The first few years at UCR were incredibly stressful and even with all the support from friends and family I found it all very difficult. In March of 2015 I decided to make some health changes. My time spent going to the local gyms and becoming part of a

health community in Riverside has helped me become mentally and physically strong, in fact, the strongest I've ever felt. With this new mentality, I was able to finish my doctorate program (while keeping my sanity and becoming a much happier person). Now, nearly a year and a half later, I have learned to manage the stress, my physical health, and have a whole new determination on living a healthier and happier life, which has all helped me make the right decisions in the final months of my doctorate program.

The people I met in the Corona and Moreno Valley gyms didn't know very much about me (for the first few months) but were incredibly friendly and made the gym and my classes feel like a second home in Riverside (the lab being my first home in Riverside). As my friends at the gym slowly learned more about me, they cheered me on as I stepped closer to finishing my doctoral program. I would like to thank all of the people I met and the few that became friends, especially Henry, Maria, Vicki, Lety, and Jenny.

I will never forget my instructors, especially Tyra for always shouting out "Dr. V!" as I walked into Zumba class, or Sylvia for announcing to all of the 50+ people in TKB that we would do an extra (5th) turbo round only "because Velveth just finished her PhD and she always wants one more" or Shawnette for coming back from her 3-week trip and noticing right away that I had moved from doing the modified moves to actually doing jumps in class (which I had practiced while she was gone!) and then calling me "smarty pants," or Linh for having a great class the morning I presented my dissertation defense. You all truly helped me feel at home in Riverside so I thank you for your support and for encouraging a new healthy lifestyle.

Completing this doctoral program and continuing on to teach at the university-level is truly a dream come true. I would not have achieved any of this without the love and support of everyone I mentioned here. Thank you so so so much ☺.

ABSTRACT OF THE DISSERTATION

Prospects of Two-Dimensional Devices: Electrical and Optical Characterization of Transition Metal Dichalcogenide Films

by

Velveth Klee

Doctor of Philosophy, Graduate Program in Materials Science and Engineering
University of California, Riverside, December 2016
Dr. Ludwig Bartels, Chairperson

Understanding the electrical and optical properties of 2D materials down to their monolayer limit is important for establishing their potential for novel applications. Prominent among 2D materials are transition metal dichalcogenides (TMDs), such as MoS2 and $MoSe_2$. These materials have attracted attention because of their intriguing properties, such as a transition from an indirect bandgap for few layers to a direct bandgap for monolayers. New synthetic routes like chemical vapor deposition (CVD) allow for high-quality, centimeter-scale growth and tuning of the direct optical gap continuously between the values of single-layer MoS_2 (1.87eV) and $MoSe_2$ (1.55eV).

In the first part of this work, we perform optoelectronic measurements of alloy devices fabricated on CVD-grown, monolayer MoS_2, $MoS_{2(1-x)}Se_{2x}$, and $MoSe_2$ islands. For all alloy compositions there is an unusual superlinear dependence of the photocurrent on light intensity. We also establish the photoconductive nature of the photoresponse,

with the photocurrent originating from recombination and field-induced carrier separation in the channel.

The study of transport characteristics of TMDs is extended to explore the effects of devices on a piezoelectric substrate as a route towards establishing fabrication processes suited for industry. In this work, we show that CVD-growth of MoS_2 monolayer films onto periodically poled lithium niobate (PPLN) is possible while maintaining the substrate polarization pattern. Electrical transport measurements indicate an inversion of the MoS_2 from *n*-type to *p*-type behavior under application of an external voltage depending on the domain orientation of the ferroelectric substrate. Sensitivity to ferroelectric substrate polarization opens the possibility for ferroelectric nonvolatile gating of TMDs in scalable devices fabricated free of exfoliation and transfer.

Optimizing CVD techniques allows for preparation of TMD films in different phases that are reported to exhibit semiconducting and metallic properties. Here, we show optical and electronic characterization of few-layer films of $MoTe_2$ in three distinct structural phases: 2H, 1T' and 1T. Depending on process parameters, either of the phases can be prepared using MoO_3 and elemental tellurium precursors. Experimental and computed Raman spectra are presented for each phase. Transport measurements validate predictions from DFT-based band structure calculations on the metallic character of the centrosymmetric 1T phase.

Table of Contents

Chapter 1 Synthesis and Characterization Techniques for 2D Transition Metal Dichalcogenides

Introduction..1

Materials, Methods, and Results...1

Figures..6

References..11

Chapter 2 Transport Characteristics of 2D Transition Metal Dichalcogenides on Patterned and Non-Patterned substrates

Introduction..12

Materials, Methods, and Results...13

Figures..20

References..28

Chapter 3 Superlinear Composition-Dependent Photocurrent in CVD-Grown Monolayer $MoS_{2(1-x)}Se_{2x}$

Introduction..29

Materials and Methods..31

Results..33

Figures..42

References..48

Chapter 4 Toward Ferroelectric Control of Monolayer MoS_2

Introduction..51

Materials and Methods..52

Results..55

Figures...64

References...67

Chapter 5 Synthesis and Characterization of Mono and Few Layer $MoTe_2$ in the 2H, 1T' and 1T Phase

Introduction..71

Materials and Methods..73

Results..75

Figures...78

References...82

List of Figures

Figure 1 6
Figure 2 7
Figure 3 8
Figure 4 9
Figure 5 10
Figure 6 20
Figure 7 21
Figure 8 22
Figure 9 23
Figure 10 24
Figure 11 25
Figure 12 26
Figure 13 27
Figure 14 42
Figure 15 43
Figure 16 44
Figure 17 45
Figure 18 46
Figure 19 47
Figure 20 64
Figure 21 65
Figure 22 66
Figure 23 78
Figure 24 79
Figure 25 80
Figure 26 81

Chapter 1

Synthesis and Characterization Techniques for 2D Transition Metal Dichalcogenides

Introduction

In this section I will present two methods for the synthesis of 2D TMDs along with characterization techniques to validate their mono- and few-layer properties. The first method presented is based on powder precursors heated in a tube furnace without the need for temperature control [1]. The second method is based on a liquid injection of chalcogen precursors that is also carried out in a tube furnace and, unlike the first method described, is temperature dependent. In this chapter, photoluminescence (PL), atomic force microscopy (AFM), and scanning electron microscopy (SEM) imaging is provided to validate the quality of the TMD films [2].

Materials, Methods, and Results

TMD Synthesis: Method 1

In the Bartels lab, MoS_2 is made via facile CVD techniques that yield growths found to be uniform in their spectroscopic properties and feature large areas that are of

monolayer thickness. By altering synthesis parameters, this facile method can also produce few-layer films.

The growth process for MoS_2 monolayers is based on the solid-source scheme of Lee et al. [3]. We use two alu- mina crucibles (Aldrich Z561738, 70 mm×14 mm×10 mm) containing MoO3 (Aldrich 99.5%) and sulfur (Alfa 99.5%) powders as our Mo and S sources, respectively (Fig. 1). These sources are placed in a quartz process tube (2" diame- ter), which is inserted in a furnace (Mellen TT12), only the center zone of which is powered. A rapid flow of nitro- gen gas (99.999%) is used to purge the tube (5.0 SCFH, 0.14 Nm3/h)), with subsequent film growth occurring at a reduced nitrogen flow rate (0.5 SCFH, 0.014 Nm3/h). The crucible containing MoO_3 is placed at the center of the heated zone, with the substrate resting directly on it. The crucible containing sulfur is placed upstream, out- side the zone of the tube furnace that was heated. Our substrate is a 3 × 3 cm piece of a boron-doped Si (110) wafer covered by a 300 nm thick layer of oxide (SUMCO). The substrate is cleaned immediately prior to growth by a piranha etch solution, formed as a mixture of 3 parts sulfuric acid and 1 part hydrogen peroxide (30%) [1].

The position of the sulfur crucible is optimized so during heat-up the sulfur melts to form a flat, uniform liquid surface at the time that the center section of the process tubes (where the MoO_3 crucible is located) reaches ~880 K, as measured by a type-K thermocouple at the outer surface of the process tube. Growth is achieved by waiting and continuing to provide power to the center section of the furnace for 3 min after the sulfur melts. Subsequently, all power to the furnace is switched off and it is left to cool

undisturbed, while the N_2 flow is continued. Thus, no temperature control of the furnace is required.

After deposition, the substrates display elongated areas hundreds of microns long and approximately 100 microns across that are continuously covered by a MoS_2 film and islands (Fig. 2). PL measurements (Fig. 3) are performed with laser excitation where a single emission peak is measured at a photon energy of 1.87 eV. This peak corresponds to the direct-gap transition of monolayer MoS_2 [4]. The continuous film and the area consisting of individual islands show the same photoluminescence characteristics. In Fig. 4, AFM shows that the film and the islands at its edge are homogeneous in height; no steps in height are found except for a small number of isolated irregular pits. No dislocation lines or 2D grain boundaries were resolved by AFM. SEM imaging at 2kV beam energy shows improved resolution of the island perimeters (Fig. 5), which appear as bright outlines in the images.

TMD Synthesis: Method 2

Our method improves on our previous CVD work by using thiophenol in methanol and diphenyl-diselenide in tetrahydrofuran as sulfur and selenium precursors, respectively. Segregration of MoS_2 and $MoSe_2$ into different films (or pure growth of the thermodynamically more stable MoS_2) is prevented by injecting the liquid precursors during MoO_3 evaporation in the process region of a tube furnace at 650° C, and apply hydrogen for carbon removal. $MoS_{2(1-x)}Se_{2x}$ alloy samples are prepared by mixing the

precursor solutions or, for low sulfur contents, by facile sulfur contamination of the $MoSe_2$ growth.

For sample preparation, a tube furnace with a 2” quartz process tube is used with nitrogen as process gas. Similar to Lee at al, MoO3 is used as a solid Mo source and 300nm SiO2/Si substrates [3]. Growth down to 30nm of oxide thickness is observed, below which single-layer films become indiscernible in standard optical microscopy. Inside the process tube, the MoO3 powder is placed on a tray made from Mo sheet and the substrate is suspended a few mm above this tray angled some 40° to face the nitrogen flow direction. Once the furnace has reached the deposition temperature, a syringe with a needle reaching to the direct vicinity of the substrate in the process tube is used to inject a small quantity (<1ml) of the sulfur/selenium source. Following injection, the tube furnace is switched off and left to cool. This procedure creates extended layers that are covered by amorphous carbon, which is visible in Raman spectroscopy, quenches the PL yield and cannot be removed with oxygen plasma or UV light without destroying the single–layer MoS_2 film. To mitigate carbon formation, we change the process gas from nitrogen to hydrogen directly after injection of the sulfur/selenium source. Sulfur-contamination of $MoSe_2$ growth can occur from sulfur desorption from the Mo source/substrate holder, if it was used in a prior growth in the presence sulfur. For a MoS1.68Se0.32 sample, a S:Se mole fraction of 0.7:1 is used reflecting the higher affinity of Mo for S than Se.

For MoS_2, nearly a continuous single-layer film covers the entire substrate with exception of the area where the oxide boat touches. For $MoSe_2$ and $MoS_{2(1-x)}Se_{2x,}$ we typically find areas up to a few mm^2 in size with homogeneous single-layer film bordered

by areas without any growth on one side and multilayer growth on the other. Fig. 3 shows room-temperature (RT) PL spectra of different compositions of $MoS_{2(1-x)}Se_{2x}$ ranging from MoS_2, with a PL energy of 1.87 eV to $MoSe_2$, with a PL energy of 1.54 eV. The spectra were acquired using excitation at 532 nm and reveal reasonably sharp and bright PL features. Also performed AFM imaging of the film of Figs. 4 after Se insertion and found it to be flat and as smooth as before (Fig. 4)

Figures

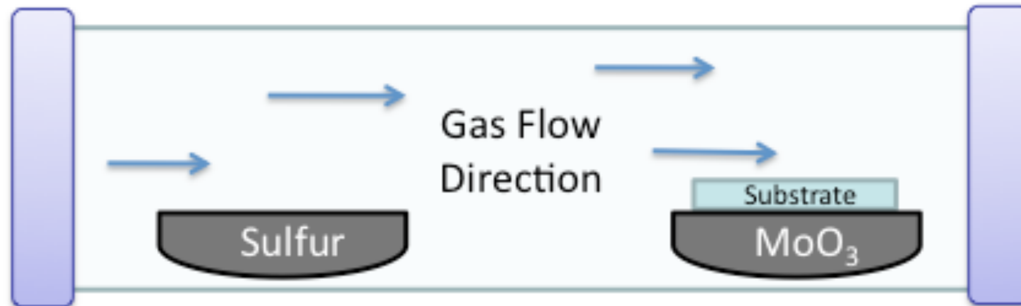

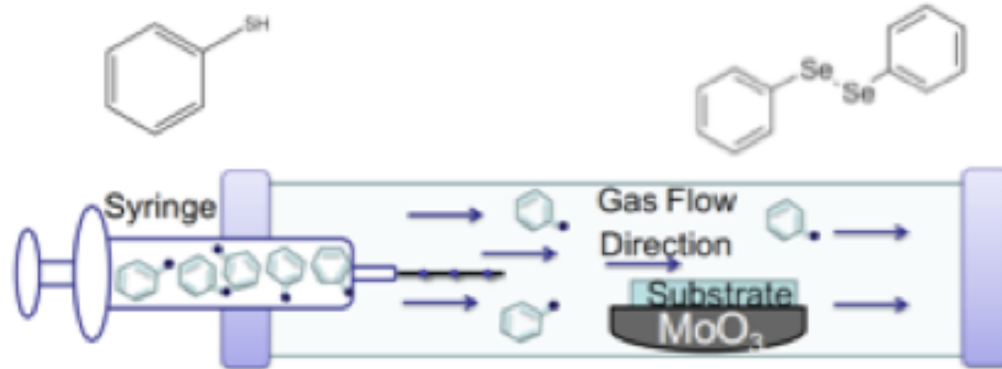

Figure 1. CVD-growth is carried out in quartz tube furnaces.

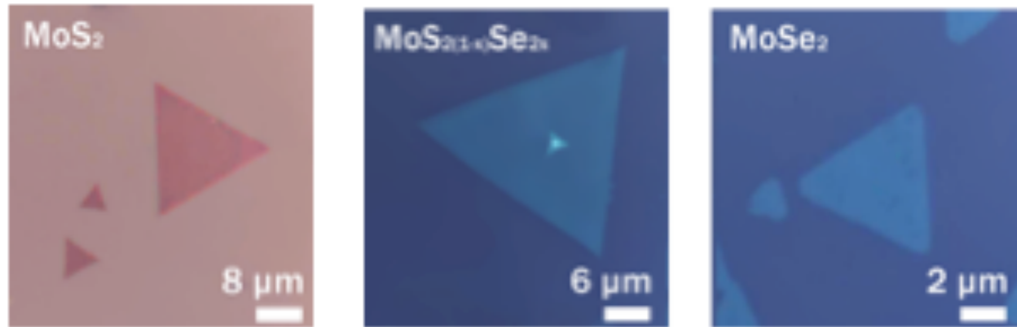

Figure 2. Single-layer islands of MoS_2, $MoSe_2$, and a mid-range alloy.

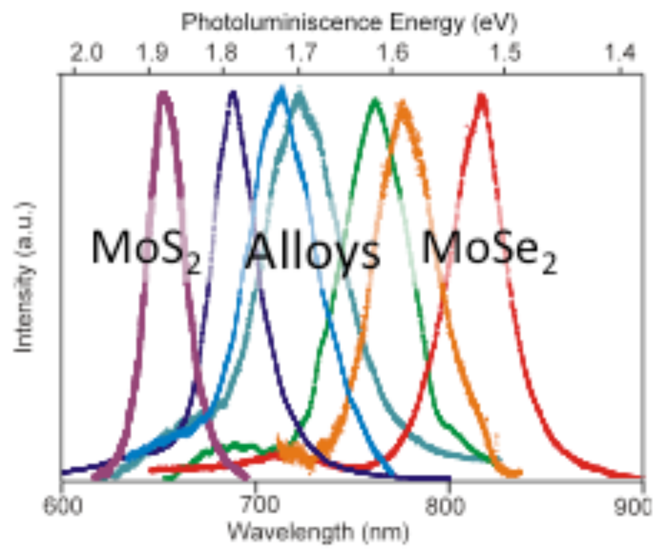

Figure 3. Photoluminescence measurements of MoS_2, $MoSe_2$ and their alloys thereof.

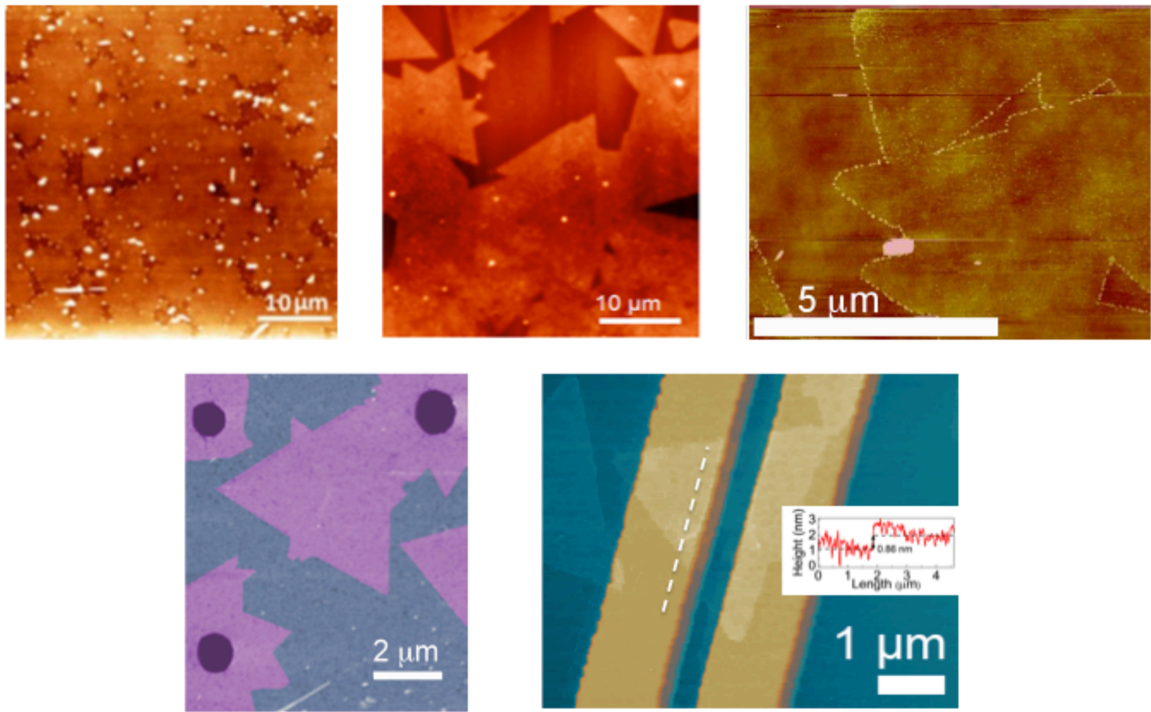

Figure 4. AFM image confirms the island shape and indicates an apparent film height of ~1nm as typically found for CVD MoS_2 islands.

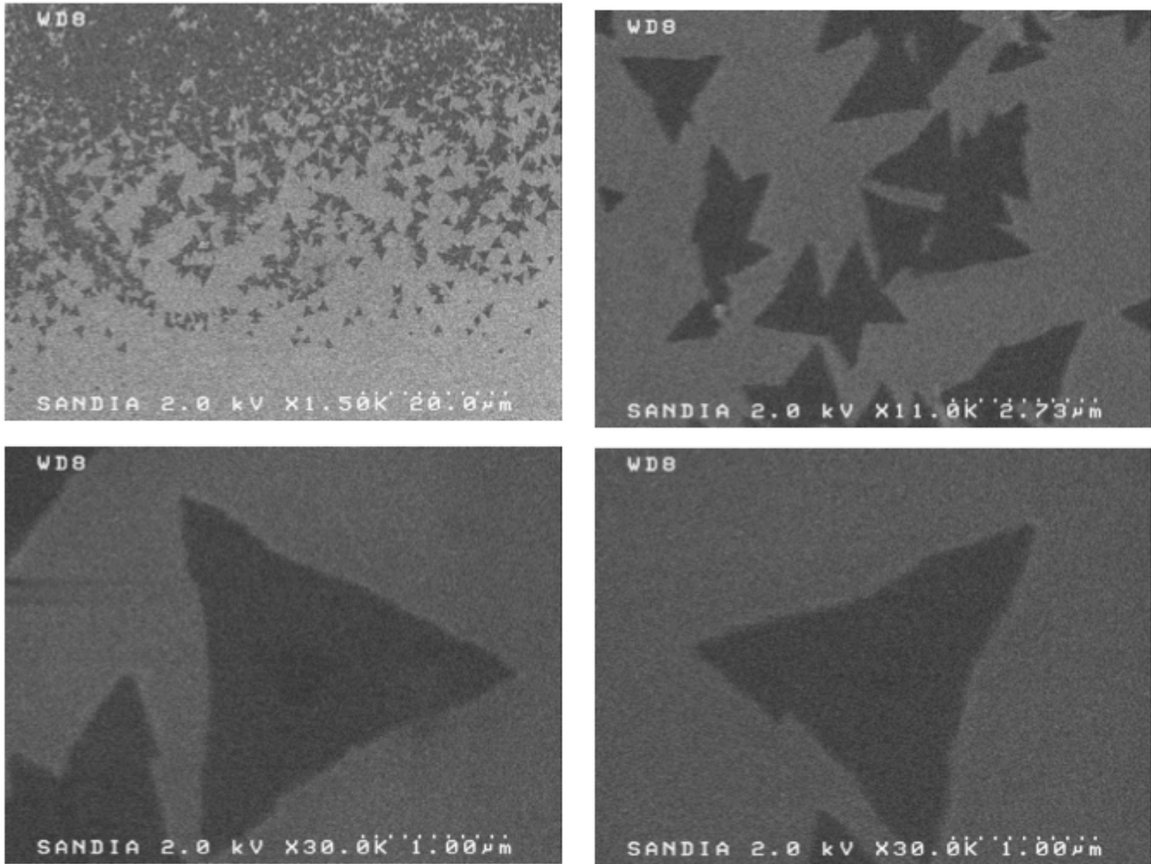

Figure 5. SEM imaging at 2kV beam energy allows us to discern the perimeters of the islands at high fidelity.

References

(1) Mann, J.; Sun, D.; Ma, Q.; Chen, J.-R.; Preciado, E.; Ohta, T.; Diaconescu, B.; Yamaguchi, K.; Tran, T.; Wurch, M.; Magnone, K.; Heinz, T. F.; Kellogg, G. L.; Kawakami, R.; Bartels, L. Facile growth of monolayer MoS_2 film areas on SiO_2. *Eur. Phys. J. B* **2013,** *86*, 1-4.

(2) Mann, J.; Ma, Q.; Odenthal, P. M.; Isarraraz, M.; Le, D.; Preciado, E.; Barroso, D.; Yamaguchi, K.; von Son Palacio, G.; Nguyen, A.; Tran, T.; Wurch, M.; Nguyen, A.; Klee, V.; Bobek, S.; Sun, D.; Heinz, T. F.; Rahman, T. S.; Kawakami, R.; Bartels, L. 2-Dimensional Transition Metal Dichalcogenides with Tunable Direct Band Gaps: $MoS_{2(1-x)}Se_{2x}$ Monolayers. *Adv. Mater.* **2014,** *26*, 1399-1404.

(3) Lee, Y.-H.; Zhang, X. Q.; Zhang, W.; Chang, M.-T.; Lin, C-T.; Chang, K.D.; Yu, Y. C.; Wang, J. T.; Chang, C.; Li, L. J.; Lin, T. W.; Synthesis of Large-Are MoS_2 Atomic Layers with Chemical Vapor Deposition. *Adv. Mater.* **2012**, *24*, 2320-2325.

(4) Mak, K. F.; Lee, C.; Hone, J.; Shan, J.; Heinz, T. F. Atomically Thin MoS_2: A New Direct-Gap Semiconductor. *Phys. Rev. Lett.* **2010,** *105*, 136805.

Chapter 2

Transport Characteristics of 2D Transition Metal Dichalcogenides on Patterned and Non-Patterned substrates

Introduction

This section will present the transport characteristics of several TMD materials grown by CVD methods (described in Chapter 1) onto patterned and non-patterned substrates. The attributes of each device structure will be discussed. The first transport characteristics presented show the *n*-type behavior of monolayer WS_2 on a flat SiO2/Si substrate; this work was part of an article published in Applied Physics Letters [1]. The second transport characteristics presented show the *n*-type and ambipolar behavior of monolayer MoS_2 and Nb-doped MoS_2, respectively. In this on-going work, a high-vacuum CVD method is used to produce monolayer MoS_2 and Nb-doped MoS_2 films; the resulting transport properties validate growth techniques and film properties across several hundred micrometers. The third transport characteristics presented show the potential transport behavior of MoS_2 grown by CVD methods across vertical pillars that are lithographically patterned onto a SiO_2/Si substrate. In this on-going work, CVD methods are used to grow monolayer MoS_2 islands and films across nanometer scale vertical channels as a pathway for mass-producing transistor-like vertical devices with fewer fabrication steps than traditionally needed.

Materials, Methods, and Results

1. Transport Characteristics of mono- and few-layer WS_2 on SiO_2/Si Substrates

The following work is taken from an article published in Applied Physics Letters and is presented here with permission from the American Institute of Physics Publishing. This collaborative work was done by me and the following students and collaborators.

Iori Tanabe,[1] Michael Gomez,[2] William C. Coley,[2] Duy Le,[3] Elena M. Echeverria,[1] Gordon Stecklein,[4] Viktor Kandyba,[5] Santosh K. Balijepalli,[5] Velveth Klee,[2] Ariana E. Nguyen,[2] Edwin Preciado,[2] I-Hsi Lu,[2] Sarah Bobek,[2] David Barroso,[2] Dominic Martinez-Ta,[2] Alexei Barinov,[5] Talat S. Rahman,[3] Peter A. Dowben,[1] Paul A. Crowell[4] and Ludwig Bartels[2]

[1]Department of Physics and Astronomy, Theodore Jorgensen Hall, 855 N 16th, University of Nebraska, Lincoln, NE 68588-0299, U.S.A.

[2] Pierce Hall, University of California - Riverside, Riverside, CA 92521, U.S.A.

[3]Department of Physics, University of Central Florida, 4000 Central Florida Blvd., Orlando, FL 32816, U.S.A.

[4]School of Physics & Astronomy, University of Minnesota, 116 Church Street S.E., Minneapolis, MN 55455, U.S.A.

[5]Elettra-Sincrotrone Trieste, S.S.14, 163.5 km, 34149 Basovizza, Trieste, Italy

Growth by chemical vapor deposition (CVD) leads to mono- and multi-layer WS_2 of very high quality, based on high-resolution angle-resolved photoemission spectroscopy (ARPES). The WS_2 samples were grown by CVD, utilizing WO_3 and elemental sulfur as precursors. In order to provide sufficient chemical potential of the tungsten precursor during growth, a high temperature of 1000 ◦C was chosen. Otherwise, the film growth

followed the procedure for MoS2 outlined in Ref [2]. Films intended for transport measurements were grown on 300 nm SiO_2/Si substrates, whereas samples for angle resolved photoelectron spectroscopy (ARPES), utilize Si substrates with a very thin (<1 nm) oxide film, so as to allow for reliable charge neutralization during measurements. Before and after ARPES measurements, the samples were characterized utilizing photoluminescence and Raman spectroscopy, as well as atomic force microscopy and optical imaging.

The ARPES experiments were performed at the 3.2 L spectromicroscopy undulator beamline of the Elettra light source at a temperature of 110 K using a photon energy of 74 eV. The incident radiation was linearly polarized (along the horizontal direction) and focused to a ~0.6 μm diameter spot by means of a Schwarzschild objective [3]. An incident angle of 45◦ with respect to the sample surface was used to optimize surface sensitivity. The ARPES data were acquired using a hemispherical electron energy analyzer with a combined energy resolution of ~50 meV and angular resolution of ±0.33◦. The sample was mounted onto a scanning stage, which enabled positioning and raster imaging with respect to the fixed photon beam. Photoelectron intensity distribution maps I(kx, ky, E) were taken from microscopic areas of the WS_2 sample by rotating the electron energy analyzer with respect to the sample using a two-axis goniometer. This approach matches the one we used to obtain the band structure of single layer WSe_2 in Ref. [4].

Figure 6(a) shows the experimental band structure of multilayer WS_2(0001) obtained from the second-derivative of the ARPES display plots. The valence band

maximum is located at the Brillouin zone center ($\bar{\Gamma}$ point) and not the zone edge ($\bar{K}$ point), in contrast to the monolayer. This finding agrees with theoretical predictions [5] and results of our calculated DFT band structure shown in Figure 6(b). We attribute the shift of the valence band maximum from the $\bar{K}$ point to the $\bar{\Gamma}$ point to the increasing width or greater interlayer splitting at the $\bar{\Gamma}$ point in multilayer WS_2, [5, 6]. Our measurements find the energy difference between the top of the valence band at the $\bar{\Gamma}$ point and at the $\bar{K}$ point, $\Delta\Gamma\rightarrow K$, to be 380±20 meV.

Simple field-effect transistors (FET) were fabricated using a single platelet of monolayer WS_2 grown on SiO_2/Si, with the doped substrate functioning as the gate. The 300 nm SiO_2 layer acted as the gate oxide and source-drain contacts were fabricated with alumina tunneling barriers. A micrograph of a typical device is shown in the inset of Figure 7. The source-drain current current-voltage characteristics, shown in Fig. 7 for many different gate voltages, indicate n-type conduction, as a current is observed only a for a sufficiently large positive gate voltage. Earlier measurements show similar findings for multilayer WS_2 and demonstrates explicitly the absence of appreciable current at negative gate voltages, similar to literature results for exfoliated WS_2 transistors.

In summary, we find from angle resolved photoemission that multilayer WS2, grown by chemical vapor deposition, is robustly n-type. This finding is in agreement with literature transport measurements on exfoliated material as well as transport measurements on the same CVD material as reported here. The band structure of CVD-grown multilayer WS2 demonstrates the material's high quality and its suitability for any WS2 application envisioned.

2. Transport Characteristics of High-Vacuum CVD-grown MoS2 and Nb-doped MoS2 Films on 300nm SiO2/Si Substrates

One focus of on-going work in the Bartels lab is to produce a high vacuum CVD method for the production of MoS_2 films with the intent of producing an industrial-scale approach. Currently, we are able to grow films that cover an entire 2×2 cm^2 silicon substrate, see Fig. 8 (size limited solely by size of the vacuum chamber). These films are of much better quality than traditionally grown CVD films (mentioned in Chapter 1). These high-vacuum CVD films are much larger and substantially more uniform; there are no areas of thick bulk material. As they are grown in vacuum, there is also no particulate matter that would dirty the substrate important for incorporating these films into industrial applications.

The system (Fig. 9) functions by passing a large amount of current through a molybdenum wire until it is white hot (~2000°C). Since molybdenum has a melting point of >2600°C, this temperature is insufficient to evaporate the molybdenum. The base pressure in my growth chamber is 10^{-7} torr, about ten orders of magnitude lower than atmospheric pressure. A sulfur source, CS_2, in introduced into the chamber to a pressure of about 10^{-5}, still 8 orders of magnitude less than atmosphere. When CS_2 molecules come into contact with the hot molybdenum wire, they dissociate into carbon and sulfur. The latter forms with molybdenum of the wire as volatile MoS_x precursors. These precipitate on the growth substrate, typically SiO_2/Si, which is held in place by a heated

filament to about 700°C (also made of molybdenum, Fig. 9) so as to adjust the substrate's temperature for optimal crystalline growth of MoS_2.

The most straightforward way to achieve ambipolar FET is doping of TMD films during growth with suitable elements. The successful high-vacuum CVD growth method for MoS_2 is extended to produce a method for the synthesis of p-type MoS_2 by using dopants such as niobium. Niobium is similar to molybdenum in size and fits perfectly in the MoS_2 hexagonal structure while having one fewer valance electron. MoS_2 is natively an n-type semiconductor because it always contains some sulfur vacancies. This means that there are electrons in the conduction band free to flow when a voltage is applied. Fig. 10 shows the response of films (grown on 300nm SiO_2/Si) to strong gate voltages applied to the underlying substrate. Transport measurements show that doping with a *p*-type material alter the electronic nature of the MoS_2 from an *n*-type to *p*-type semiconductor creating holes in the valence band which can carry a current.

Transport Characteristics of CVD-grown Monolayer MoS_2 Islands and Films on Lithographically Patterned Vertical Devices

Two-dimensional transition metal dichalcogenides are promising new materials to augment silicon in novel device architectures because of their direct-bandgap and semiconducting properties at the monolayer limit, combined with pronounced spin-splitting in the valence band. Through CVD methods, our lab works on the synthesis of

TMD monolayer single-island as well as continuous films. Unlike many other direct band gap materials, TMDs grow on SiO_2/Si without the need for epitaxial match or epitaxially precise interfaces, rendering their integration very facile. Their 2D nature opens up the opportunity for entirely novel manufacturing paradigms: 3D materials like poly-silicon or oxide can be deposited largely across wafer-scale areas, even if the underlying substrate is structured; in contrast, for 2D materials like TMDs it only makes sense to deposit monolayer (or few-layer) material and if the substrate is structured then this film will grow aligned conformal to the substrate (like a blanket deposition).

This blanket-like deposition is a challenge because it introduces another level of complexity in the fabrication of devices out of 2D materials. On the other hand, it is a great opportunity because this style of growth and device fabrication illustrates that if, for instance, a vertical transistor channel from a TMD material is desired, then it is sufficient to grow a conformal single-layer TMD film into the vertical substrate region that supports the channel. There is no need for and no benefit in developing/applying growth procedures that cover wafer scale substrate with a single-domain TMD film. It is enough (and also most useful) to come up with methodologies that are capable of growing a domain-boundary-free nanoscale section of TMD into the desired channel region. Such self-aligned growth of TMD materials onto pre-patterned substrates will result in a large array of working nano-sized transistors at a minimal number of fabrication steps.

On-going efforts in the Bartels group are to develop a procedure for the growth of TMD films on the vertical region between the top and the bottom of micron-scale pillars lithographically fabricated on a SiO_2/Si substrate. (Fig. 11 and 12) In concurrent work,

research also explores the seeding of TMD films by means of lithographic patterning of the substrate. These two approaches are combined towards targeted growth of TMD materials at specific locations on a patterned substrate. Preliminary transport (Fig. 13) measurements show that self-aligned fabrication of devices is possible. What remains is to optimize the materials that make up the pillar structure so that en effective under-cut or continuous SiO_2 (or any other dielectric) remains to allow for gating of the material hanging on the side of the pillar.

Figures

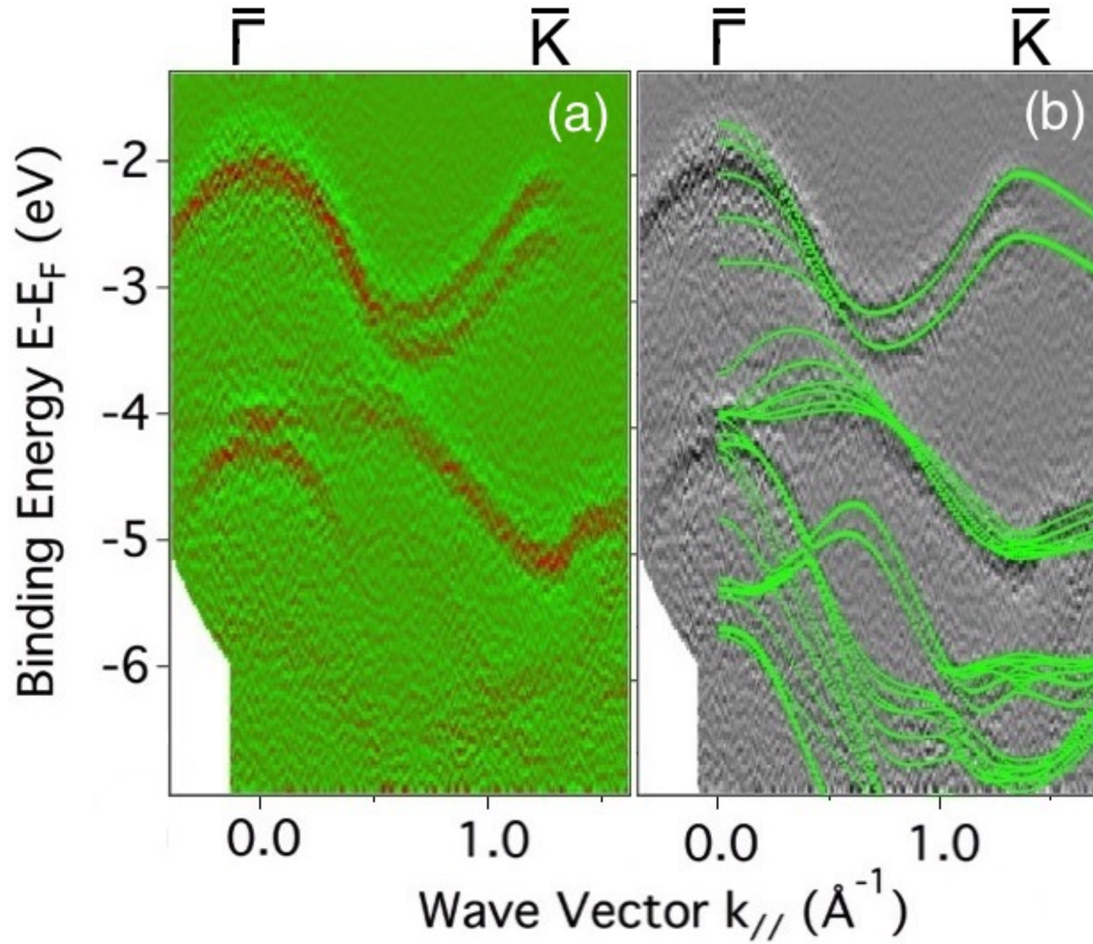

Figure 6. (a) The second-derivative image of the experimental band structure of multiple layers (five or more layers) of WS_2 obtained by High-resolution ARPES along the Γ-K high symmetry direction and (b) the comparison with theoretical calculations overlaid as dashed green lines. The photon energy is 74 eV. The splitting due to the spin-orbit coupling in the valence band near the K point is found to be approximately 420 ± 2 meV.

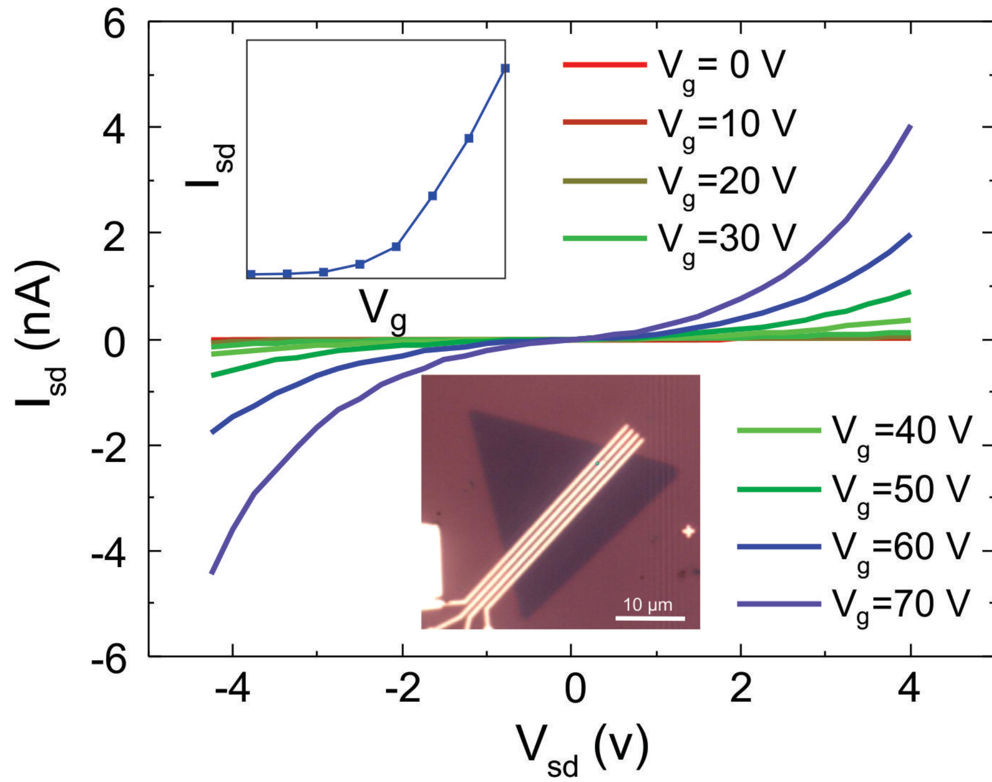

Figure 7. Local gate control of the WS_2 monolayer transistor. I_{sd} – V_{sd} curves recorded for different values of V_g ranges from 0 to 70 V.

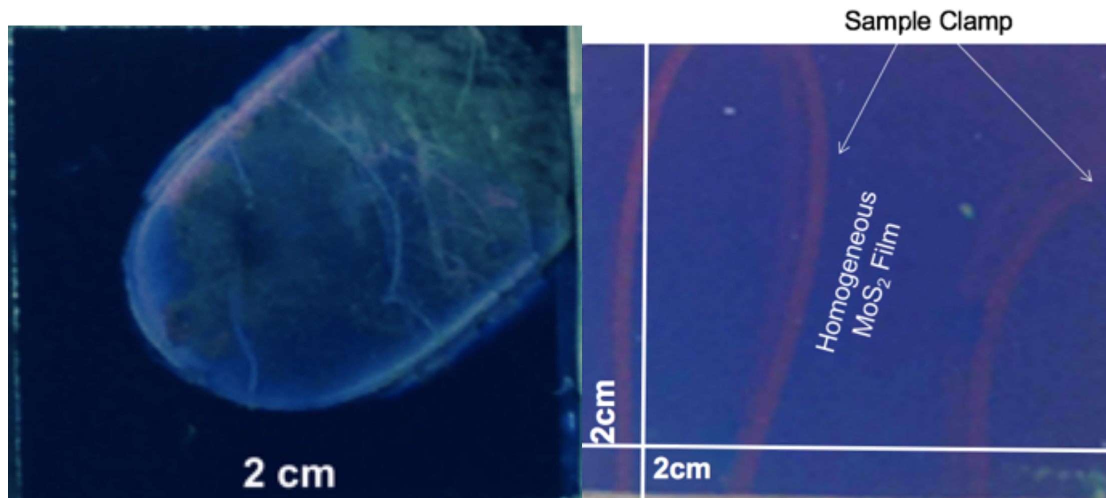

Figure 8. MoS_2 film grown by high-vacuum CVD.

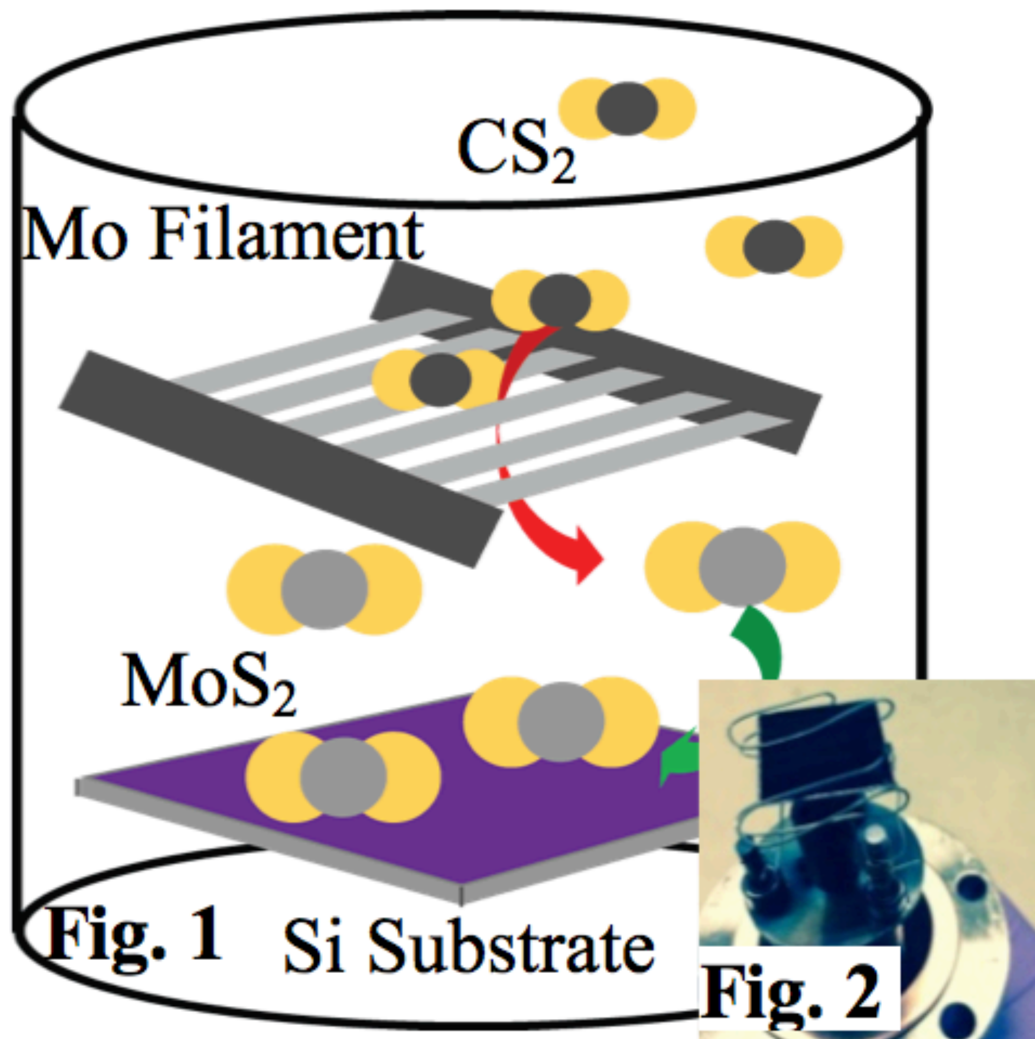

Figure 9. Schematic representation of our technique for large-area homogeneous TMD growth. (right) Preliminary indication of ambipolar response of Nb-doped MoS_2 films

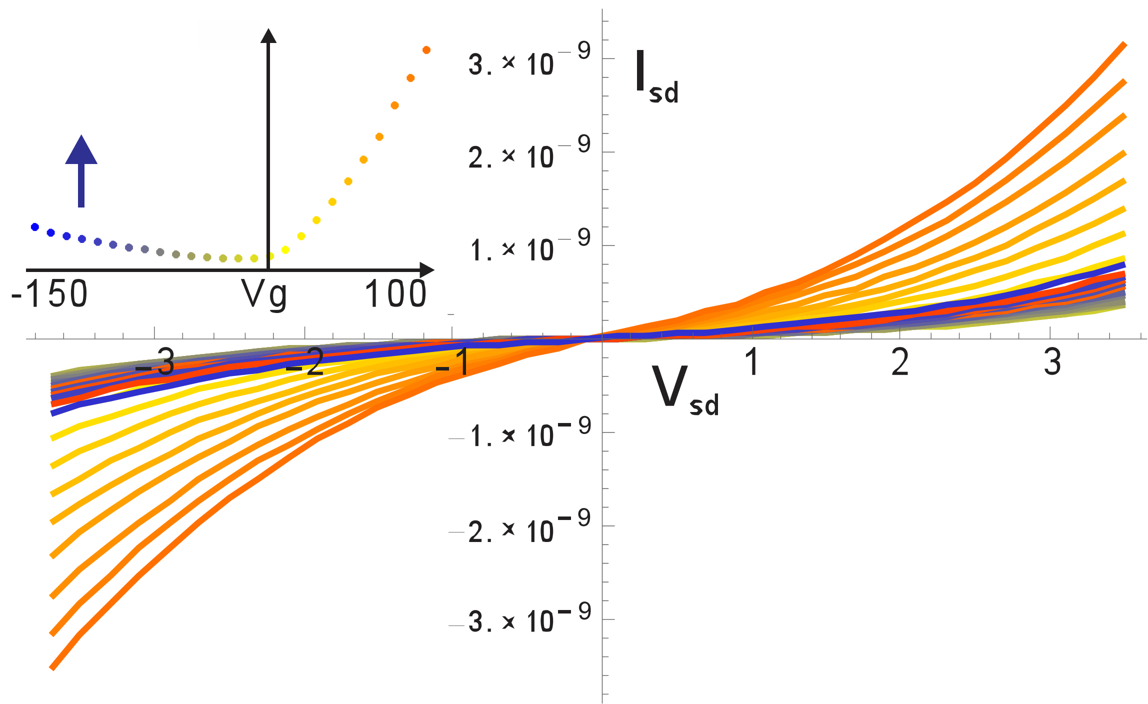

Figure 10: First signs of ambipolar behavior of a Nb-doped MoS_2 film produced. The very high voltages are required because of back-gating through a thick oxide layer.

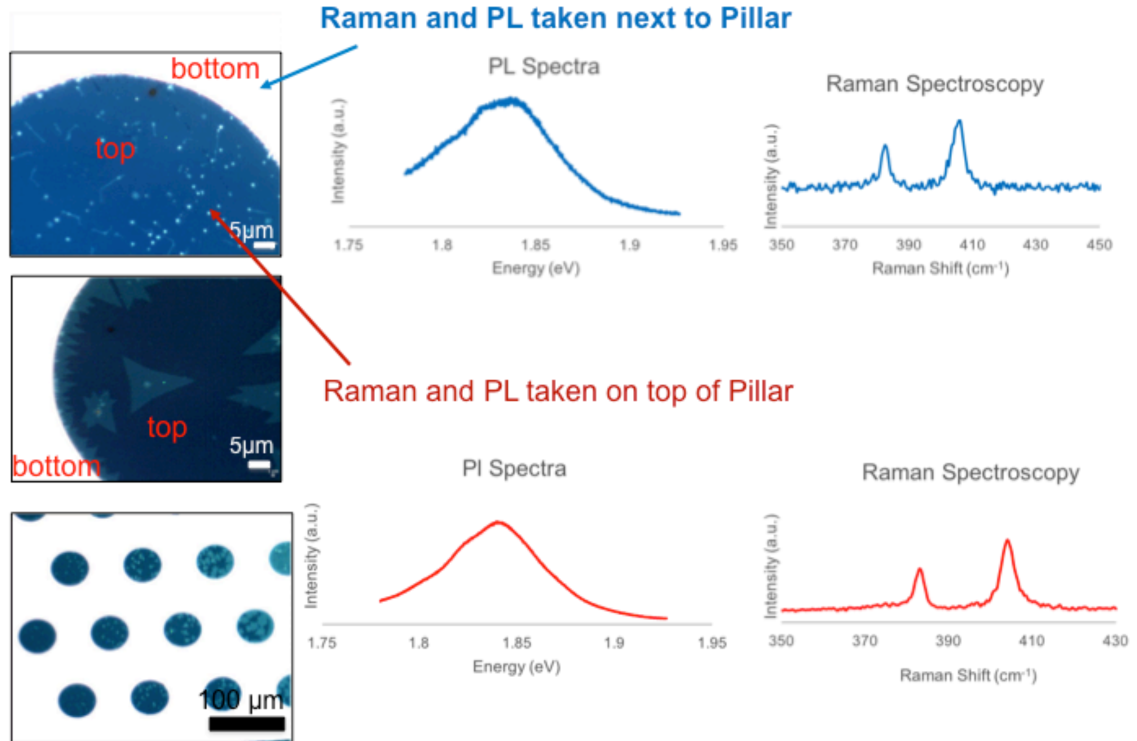

Figure 11. Pillars lithographically patterned and fabricated onto SiO2 substrates. MoS2 is grown by CVD methods and produces characteristic PL and Raman peaks.

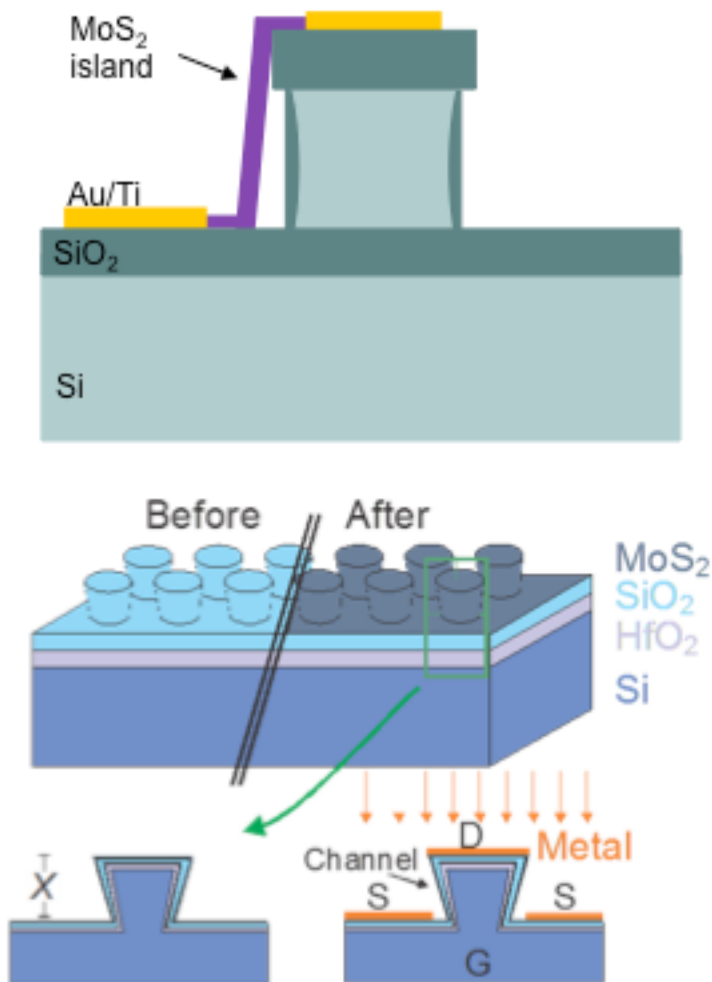

Figure 12. Schematic of side-view of pillar structure with MoS_2 growth and metal contacts. This is a vertical device.

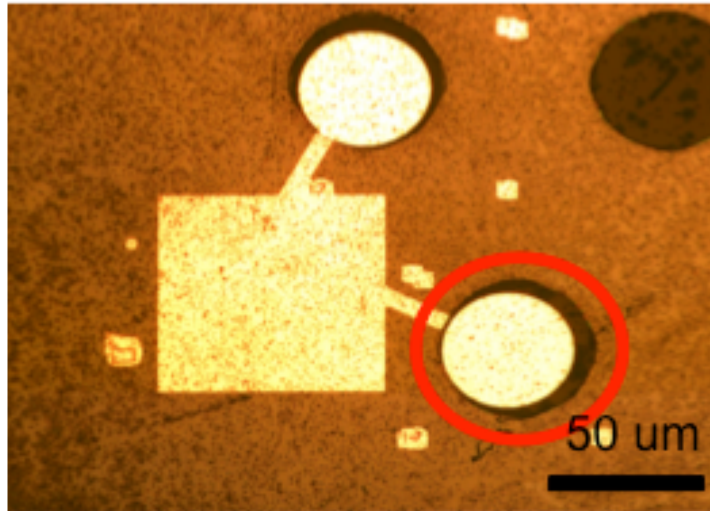

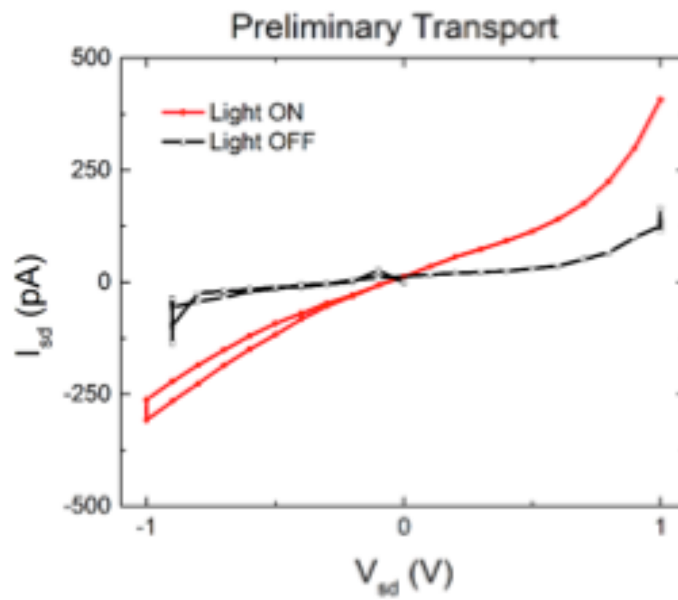

Figure 13. Preliminary transport measurements of vertical devices with MoS_2 as the channel material.

References

(1) Tanabe, I.; Gomez, M.; Coley, W. C.; Le, D.; Echeverria, E. M.; Stecklein, G.; Kandyba, V.; Balijepalli, S. K.; Klee, V.; Nguyen, A.; Preciado, E.; Lu, I-H.; Bobek, S.; Barroso, D.; Martinez-Ta, D.; Barinov, A.; Rahman, T. S.; Dowben, P. A.; Crowell, P.; Bartels, L. Band Structure Characterization of WS_2 Grown by Chemical Vapor Deposition. *Appl. Phys. Let.* **2016**, 108, 252103.

(2) Mann, J.; Sun, D.; Ma, Q.; Chen, J.-R.; Preciado, E.; Ohta, T.; Diaconescu, B.; Yamaguchi, K.; Tran, T.; Wurch, M.; Magnone, K.; Heinz, T. F.; Kellogg, G. L.; Kawakami, R.; Bartels, L. Facile growth of monolayer MoS_2 film areas on SiO_2. *Eur. Phys. J. B* **2013,** *86*, 1-4.

(3) Dudin, P.; Lacovig, P.; Fava, C.; Nicolini, E.; Bianco, A.; Cautero, G.; Barinov, A.; Angle-resolved photoemission spectroscopy and imaging with a submicrometre probe at the SPECTROMICROSCOPY-3.2L beamline of Elettra *J. Synchrotron Radiat.* **2010**, 17, 445–450.

(4) Le, D.; Barinov, A.; Preciado, E.; Isarraraz, M.; Tanabe, I.; Komesu, T.; Troha, C.; Bartels, L.; Rahman, T. S.; Dowben, P.A.; Spin-orbit Coupling in the Band structure of Monolayer WSe_2 *J. Phys.: Condens. Matter* **2015**, 27, 182201.

(5) Kuc, A.; Zibouche, N.; Heine, T.; Influence of quantum confinement on the electronic structure of the transition metal sulfide TS_2 *Phys. Rev. B* **2011**, 83, 245213.

(6) Kosmider, K.; Fernandez-Rossier, J.; Electronic Properties of the MoS_2-WS_2 Heterjonuction. *Phys. Rev. B* **2013**, 87, 075451

Chapter 3

Superlinear Composition-Dependent Photocurrent in CVD-Grown Monolayer $MoS_{2(1-x)}Se_{2x}$

The following is taken from an article published in Nano Letters and is presented here with kind permission of American Chemical Society Publications. This collaborative work was performed by me and the following students and collaborators.

Velveth Klee[1], Edwin Preciado[1], David Barroso[1], Ariana Nguyen[1], Chris Lee[1], Kristopher J. Erickson[2], Mark Triplett[2], Brandon Davis[1], I-Hsi Lu[1], Sarah Bobek[1], Jessica McKinley[1], Joseph P. Martinez[1], John Mann[1], A. Alec Talin[2], Ludwig Bartels[1*] & François Léonard[2*]

[1]Materials Science & Engineering Program and Departments of Chemistry and Mechanical Engineering, University of California, Riverside, California 92521, USA

[2]Sandia National Laboratories, Livermore, California 94551, USA

Introduction

Transition metal dichalcogenides (TMDs) have emerged as a new class of two-dimensional materials that are promising for electronics and photonics. In this work, we use spatially resolved photocurrent measurements on devices consisting of CVD-grown monolayers of TMD alloys spanning MoS_2 to $MoSe_2$ to show the photoconductive nature of the photoresponse, with the photocurrent dominated by recombination and field-induced carrier separation in the channel. Time-dependent photoconductivity measurements show the presence of persistent photoconductivity for the S-rich alloys,

while photocurrent measurements at fixed wavelength for devices of different alloy compositions show a systematic decrease of the responsivity with increasing Se content associated with increased linearity of the current–voltage characteristics. A model based on the presence of different types of recombination centers is presented to explain the origin of the superlinear dependence on light intensity, which emerges when the nonequilibrium occupancy of initially empty fast recombination centers becomes comparable to that of slow recombination centers. Thermal effects are ruled out by complementary measurements of thermal transport using infrared imaging.

Initial studies focused primarily on phototransistors based on mechanically exfoliated single- and few-layer MoS_2 [7-10]. In contrast to our results, these devices produce a photocurrent that is linearly dependent on laser power at low powers and becomes sub-linear with increasing power [7, 8]. A recent study on few-layer MoS_2 phototransistors also confirms the sub-linear dependence of the photocurrent on laser power and attributes the dominant photoresponse to a separation of photoexcited carriers caused by a built-in or external electric field [4,9]. This is contrary to a previous study that reports photocurrent generation in single-layer MoS_2 dominated by the photothermoelectric effect (PTE) [10]. A recent study reports on phototransistors based on single-layers of MoS_2 synthesized by chemical vapor deposition (CVD); these results also show sub-linear dependence of the photocurrent on laser power [11]. An open question is whether the above results extend to other TMDs, and in particular to the recently discovered $MoS_{2(1-x)}Se_{2x}$ alloys grown by CVD [5, 6, 12, 13].

In this work, we address this question through optoelectronic characterization of alloy devices fabricated on a range of CVD-grown, single-layer MoS_2, $MoS_{2(1-x)}Se_{2x}$, and $MoSe_2$ islands. We find that for all alloy compositions there is an unusual superlinear dependence of the photocurrent on light intensity. Through a series of experiments we establish the photoconductive nature of the photoresponse, with the photocurrent originating from recombination and field-induced carrier separation in the channel. By measuring devices across the full range of alloy compositions we report that increasing Se content systematically decreases the photoresponsivity in conjunction with a transition from notably non-linear to nearly-linear current-voltage characteristics. Finally, a model based on different types of recombination centers is presented; it shows the emergence of superlinearity in the presence of slow and fast recombination pathways through their non-equilibrium occupancy.

Materials and Methods

Single-layer $MoS_{2(1-x)}Se_{2x}$ alloys were grown by CVD in a tube furnace at 650°C on a SiO_2/Si substrate (100 nm thickness of SiO_2, heavily doped Si). For MoS_2, MoO_3 powder and elemental sulfur were used for the metal and chalcogen source, respectively. For $MoSe_2$ and alloys, the chalcogen sources are thiophenol and diphenyl-diselenide; the amount of each source is varied to adjust the sulfur/selenium ratio, as described in detail in previous publications [4, 5]. Raman and photoluminescence measurements were used to characterize the alloys with regards to their optical bandgap and to confirm the

monolayer nature of the material. The photoluminescence peak varies from 1.55 eV for $MoSe_2$ to 1.85 eV for MoS_2, with intermediate values attained for intervening alloy compositions. A linear variation of bandgap with composition is assumed throughout this work [5, 12, 13].

Electronic devices were fabricated by patterning PMMA/MMA bilayer resists using e-beam lithography. Ti/Au (2 nm/ 50 nm) electrodes were deposited by electron beam evaporation. We verified that device fabrication did not affect the material by comparing the photoluminescence before and after fabrication. Devices described throughout this manuscript have channel lengths between 0.5 μm and 5 μm, and they continuously span the compositional space between MoS_2 and $MoSe_2$. Dozens of devices were fabricated, characterized, and measured for this study. All devices addressed in this manuscript were fabricated on regular triangular single-layer islands with side lengths around 15 μm, which are typical of single-crystalline material [4]. A representative optical image of a $MoS_{2(1-x)}Se_{2x}$ device is shown in the inset of Fig. 14a. An AFM linescan in the channel area gives a step height of ~0.85 nm going from the SiO_2 substrate to the $MoS_{2(1-x)}Se_{2x}$ island, confirming the monolayer nature of the material (Supporting Information). On all devices, electrical measurements yield very little current for source-drain biases up to ±2 V, even when the devices were gated with up to ±60 Volts through the heavily doped Si substrate (resistivity 0.005 Ω-cm), the exception being some pure MoS_2 devices, as shown in the Supporting Information. All measurements were performed in ambient.

We use scanning photocurrent microscopy (SPCM) to characterize the optoelectronic properties of the devices. The beam from a red HeNe laser (633nm) was fed into a microscope and focused on the devices using a 50X, NA=0.55 objective, and the current was measured using a DL 1211 current pre-amplifier and a probe station. As shown in the Supporting Information, the spot diameter at half-maximum is about 1.3 μm. Different beam powers (measured by replacing the sample with a Newport 818 photodetector) were realized by appropriate filters placed between the laser source and the microscope. A computer-controlled stage was used to move the devices in 50 nm steps with respect to the laser beam while the current was recorded. The intensity of the reflected light was collected simultaneously to create spatially-resolved reflection images, in which the metallic electrodes appear bright compared to the moderately reflective SiO_2/Si substrate. In addition to regular optical images, the presence of the $MoS_{2(1-x)}Se_{2x}$ island can readily be discerned from the substrate (see insets in Figs 14a,e) by a drop in reflected power of ~6%.

Results

Figure 1 shows representative SPCM maps taken at zero bias and at biases of ±1 V for two devices consisting of $MoS_{1.6}Se_{0.4}$ and $MoS_{0.4}Se_{1.6}$ single-layer islands. We applied a laser power of 1310 μW in a near diffraction-limited spot resulting in a power density of ~80 kW/cm^2. At zero bias, very small photocurrent spots typically on the order of hundreds of picoamps are observed which are most often located near the electrodes as

in Fig. 14a, but are also sometimes seen in the channel (Fig. 14e). These very small currents could originate from the presence of band-bending at the contacts [9] and/or due to the photothermoelectric effect [10]. Under bias of either polarity, the photocurrent increases by several orders of magnitude to hundreds of nanoamps for S-rich compositions (Fig. 14b,c) and to tens of nanoamps for Se-rich compositions (Fig. 14f,g). While the laser spot size is comparable to the channel length, it is still possible to see in these measurements that the maximum photocurrent is observed in the channel, either closer to the electrode edges (Fig. 14d) or in the middle of the channel (Fig. 14h). Additional SPCM maps for longer channel devices and for MoS_2 and $MoSe_2$ can be found in the Supporting Information, and show that for MoS_2 and sulfur-rich alloy devices the photocurrent maxima are located near the negatively biased electrode, as would be expected for a system of back-to-back Schottky diodes with band-bending in the channel near the electrodes [9].

The SPCM maps of Fig. 14 were acquired left to right (fast scan direction) and top to bottom (slow scan direction). We observe some apparent photocurrent even when the excitation beam has passed the area between the electrodes, especially for the S-rich composition. This artifact is caused by a slow photocurrent response. Fig. 15a shows the time dependence of the photocurrent for a 5μm channel MoS_2 device for a bias of +1 V when the laser is focused in the channel near one of the electrodes. The photocurrent dynamics are exceedingly slow, with rise times (90% of maximum current) and decay times (10% of maximum current) of 12 min and 10 min, respectively. Introducing selenium accelerates the photoresponse to a few minutes for $MoS_{1.2}Se_{20.8}$ (Fig. 15b) until

the response exceeds the limit of the pre-amplifier (Fig. 15b inset). The bleeding observed in the SPCM images for the S-rich material originates from the slow photocurrent decay and is observed in the fast scan direction (see Supporting Information for detailed discussion). In addition, a photocurrent outside of the area between the electrodes can originate from fringe fields from the electrodes (experimental results and simulations are presented in the Supporting Information). Persistent photoconductivity as in Fig. 15a is well-known to arise due to charge traps [14]. In such systems the photocurrent decay can be described with a stretched exponential function $I_{ph}(t) = I_{ph}^{0} \exp\left[-\left(t/t^{*}\right)^{\beta}\right]$; the inset in Fig. 15a shows an excellent fit of this function to the experimental data, giving an exponent (Note that a simple exponential decay is not able to describe the photocurrent dynamics.)

The channel length dependence of the photocurrent (Fig. 15c,d) provides us with important insight into the photocurrent mechanism: for a photoconductive device, the photocurrent is expected to decay exponentially with channel length L for channels longer than the diffusion length L_D (where D is the diffusivity and τ is the recombination time), $I_{ph} = I_0 \exp\left(-L/L_D\right)$. From the strong, consistent channel length dependence of the data in Fig. 15d we obtain by least-squares fitting to an exponential function a diffusion length of 0.88±0.06 μm for the sulfur rich material and of 0.45±0.01 μm for the selenium-rich material (the error bars reflect the fit error only). The shorter diffusion length for the selenium-rich material is consistent with the faster photocurrent decay shown in Fig. 15b.

Figure 16 explores the photoresponse at different excitation intensities for a range of $MoS_{2(1-x)}Se_{2x}$ compositions. The samples proved to be stable under prolonged exposure even to the highest laser power shown in this set (see Supporting Information and Fig. 15a). Two trends can readily be discerned: 1) there is an overall decrease of photocurrent as the S content decreases, and 2) the I-V curves become progressively more linear with increasing Se content. Moreover, we also observe a non-linear dependence of the photocurrent on the excitation power that will be discussed later on. (Note that at zero bias, the photocurrent is close to zero in these figures, being due only to the small currents shown in Fig. 14a,e).

We first discuss the origin of the illumination-dependence of the I-V curves (Fig. 16). We note that there is practically no photocurrent at zero bias, and an increasing slope with increasing light intensity. This type of behavior can originate both from photoconductive or bolometric effects but it is inconsistent with a photothermoelectric effect which typically involves a photocurrent at zero bias and no change in slope [15] as the light intensity is increased. A photothermoelectric effect is further ruled out by the magnitude of the current at 1V bias, which even assuming the largest measured[10] Seebeck coefficient for MoS_2, would require a temperature gradient on the order of 10^6 K, an unrealistic value. The spatial location of the photocurrent maxima near the negative electrodes and the change of this location with inversion of the bias voltage suggests a photoconductive mechanism due to the presence of electric fields in the channel[9], in contrast to a bolometric effect. To further rule out the latter, we measured the temperature dependence of the dark I-V characteristics of a MoS_2 device as shown in

Fig. 17a. As expected, the current increases with increasing temperature; however, the increase in current is small. 400K of equilibrium temperature generates a dark I-V current of 80 pA compared to greater than 1 μA measured with the largest laser intensity, i.e. four orders of magnitude difference. An upper bound for the temperature increase during laser illumination can be obtained by assuming uniform illumination and balancing the heat input with the heat dissipation to the substrate. Then a temperature increase results where *P* is the laser power and *G* is the heat transfer coefficient between the TMD material and the substrate. Values of $G \approx 10^7$ W/m^{2}K have been extracted based on studies of heat dissipation in MoS_2 transistors, [16] about an order of magnitude lower than for graphene. Using the lower value, we obtain a temperature increase of 80K for the largest laser intensity used in this work, where our equilibrium heating yields less than 10^{-4} of the photocurrent. To further support the claim that the temperature rise is too small to lead to a significant bolometric effect, we measured the temperature rise during illumination by focusing a red Krypton laser on a region with extended (mm scale) coverage of single-layer MoS_2 on Si/SiO_2[4,5] The laser was focused on the surface, and the temperature profile was measured with an Inframetrics 760 infrared camera with 10 μm resolution. As shown in Figs. 17b,c, the focused laser illumination leads to a temperature rise at the point of excitation which decays over a distance of a few hundred microns. However, the maximum temperature rise is small, reaching only 4K under illumination with 0.31 W (~2.5 MW/cm^2, i.e., more than thirtyfold of that used for the photocurrent measurements). Because most of the optical absorption occurs in the Si substrate (we measured about 6% additional

absorption at the location of single-layer MoS_2), the IR camera measures predominantly the temperature in the Si substrate. As discussed in the Supporting Information, because of the heat exchange between the Si and the MoS_2, the temperature of the MoS_2 is directly linked to that in the Si by the thermal resistances of the SiO_2 and the MoS_2/SiO_2 interface. At the laser power used for the optoelectronic experiments, we estimate a temperature rise of about 7 K in the MoS_2, much too small to lead to a significant bolometric effect. Finally, the temperature increase at the laser spot can also be obtained by analyzing Raman spectra as a function of laser power, which gives a temperature increase of 16K for the largest laser intensity.

Having established the photoconductive nature of the optoelectronic response, we now discuss the power dependence. Figure 18 shows the photocurrent measured at a bias voltage of 2V as a function of the excitation power for three different alloy compositions. Remarkably, the photocurrent shows a pronounced and unusual superlinear dependence on the excitation power, a behavior that is also observed for different bias voltages. The superlinear dependence on laser intensity is in contrast to previously reported results on exfoliated[8, 9] and CVD-grown[11] MoS_2 where the behavior was found to be sub-linear. The difference may be due to the lower optical intensities used in these studies, as well as the properties of the materials.

Indeed, as discussed above, the sensitivity of a photoconductive device is usually determined by a combination of carrier excitation, separation, recombination, and diffusion. Despite all of these processes, the power dependence of the photocurrent is usually simple: it is linear at small power with a cross-over to sub-linear behavior at

larger powers. Superlinear photocurrents are relatively rare (see for example Refs [17-20]), and few theoretical models exist that predict superlinear behavior even in bulk materials [21-23]. All of these theories require the presence of recombination centers of different energies and capture cross-sections. A simplified description of the process involves initially empty and filled intragap states close to the conduction band and valence band, respectively. At increased laser intensity, the occupancy of these centers changes due to shifts in the quasi-Fermi-levels, resulting in an increased carrier lifetime. In our system, the potential origins of the intragap states include different defect types in CVD-grown TMDCs as shown by recent experimental and theoretical analysis[24,25], edges in CVD-grown TMDC islands, which give rise to a metallic (potentially magnetic) edge state that has been discussed in the context of chemical catalysis[24-27], or interactions with the substrate, which are known to affect the photoluminescence yield and, thus the exciton dynamics[1, 2].

To illustrate the emergence of superlinear photocurrent, we implemented a model based, for reason of simplicity, on the presence of three types of recombination centers, as illustrated in Fig. 19a. This is the simplest model that shows superlinear behavior without invoking divalent centers. We are not implying that all alloys measured here have this particular number and energy-distribution of centers; superlinear behavior can also arise for more general distributions of slow and fast centers, including continuous distributions[23]. In our model, centers of type 1 (density N_1) are located near the valence band and have a large hole capture cross-section (σ_{1h}), but a small electron

capture cross-section (σ_{1e}). Centers of type 2 and 3 are considered to have high capture cross-sections for both holes and electrons, and are located near midgap and near the conduction band, respectively. In the dark, the Fermi level is located above centers 1 and 2, but below centers 3 (this is consistent with the low conductivity observed in our devices in the dark). During illumination, the free hole and electron concentrations increase, and their respective quasi Fermi levels (E_F^p and E_F^n) move closer to the valence and conduction band edges. At high enough intensity, the initially empty centers 3 become partially filled and the recombination rate drops rapidly, signaling the onset of superlinearity.

The above model was implemented numerically by solving coupled rate equations for the occupancy of the three types of centers as a function of light intensity, including optical and thermal generation, as well as recombination. The model is presented in detail in the Supporting Information. Figure 6b shows the calculated photocurrent as a function of light intensity for the case $N_1 = N_2 = N$ and $N_3 / N = 0.01$, assuming $\sigma_{1h} = \sigma_{2h} = \sigma_{2e} = \sigma_{3h} = \sigma_{3e} \equiv \sigma$ and varying the ratio σ_{1e} / σ. When the capture cross-section for centers 1, 2, and 3 are equal, the photocurrent depends linearly on the light intensity; however, as the capture cross-section for electrons in center 1 decreases, a superlinear behavior emerges, which can become quite pronounced. Figures 19c,d show the calculated occupancy of the three centers and the recombination rate as a function of light intensity. For low intensity, centers 3 are mostly empty, while centers 1 and 2 are mostly occupied, and the recombination rate is dominated by centers 3 (barely visible in

Fig. 19d, note linear scale). As the light intensity increases, the occupancy of centers 3 increases, while centers 2 become partially empty, and the recombination traffic is mostly through centers 2. In this region the photocurrent is linear with light intensity. Upon further increase in intensity, the density of empty centers 1 is comparable to those in centers 2 and 3, and the recombination rate drops rapidly with intensity, leading to superlinear photocurrent.

In summary, we report on the optoelectronic characteristics of CVD-grown monolayer alloys that span the composition range from MoS_2 to $MoSe_2$. Our measurements show significant decrease of the photocurrent at fixed wavelength for Se-rich alloys compared to S-rich ones along with decreased diffusion length of photogenerated carriers. We find a photoconductive response that is characterized by an unusual superlinear dependence of the photocurrent on the illumination intensity. In combination with recent reports of high mobility[28] and high sensitivity of MoS_2[8], it may suggest potential for optoelectronic application of the films under investigation. Importantly, our results indicate the presence of uncommon non-equilibrium photophysics in these systems, opening a number of intriguing questions regarding the nature and control of such phenomena.

Figures

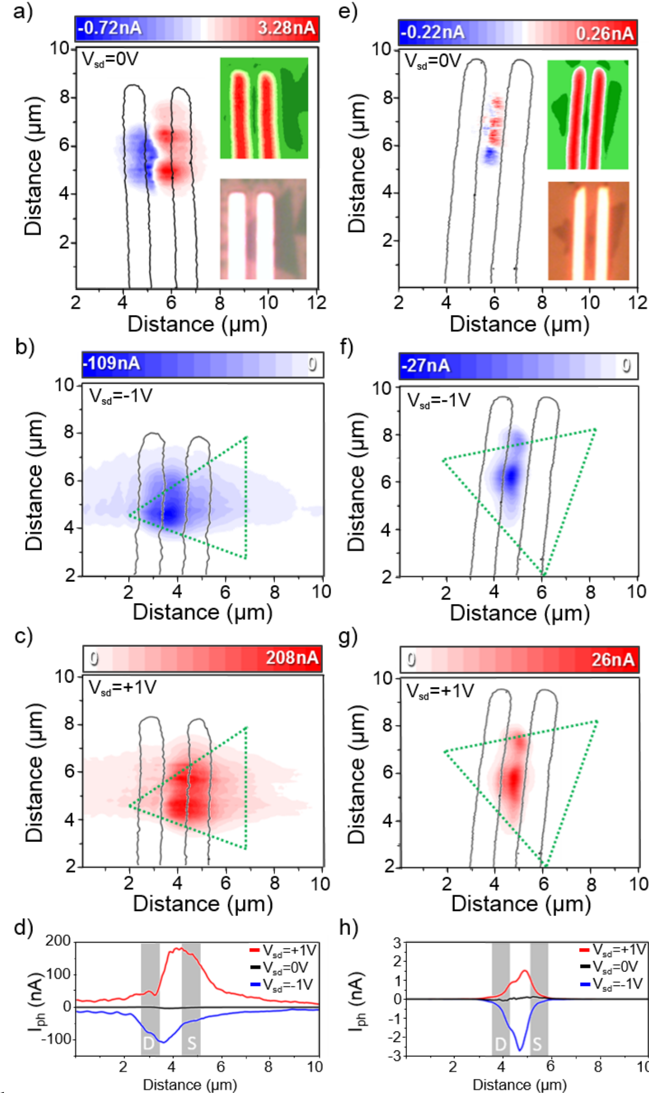

Figure 14. (a-c) Photocurrent images for a single-layer $MoS_{1.6}Se_{0.4}$ (E_g=1.80 eV) device at (a) V_{sd} = 0 V, (b) V_{sd} = -1 V, and (c) V_{sd} = +1 V. The bottom insets in (a,e) are optical images of the devices, and the top ones are the reflection images. The dotted green lines denote the outline of the TMD island in each plot. The black outlines are the electrode edges extracted from the reflection images. (e-g) Photocurrent images for a $MoS_{0.4}Se_{1.6}$ device (E_g=1.62 eV). (d,h) Photocurrent line profiles extracted from the photocurrent images. Drain and source electrodes are labeled “D” and “S” respectively. In all panels a red laser is used with a power of 1310 μW, and the voltage is applied to the drain electrode on the left hand side.

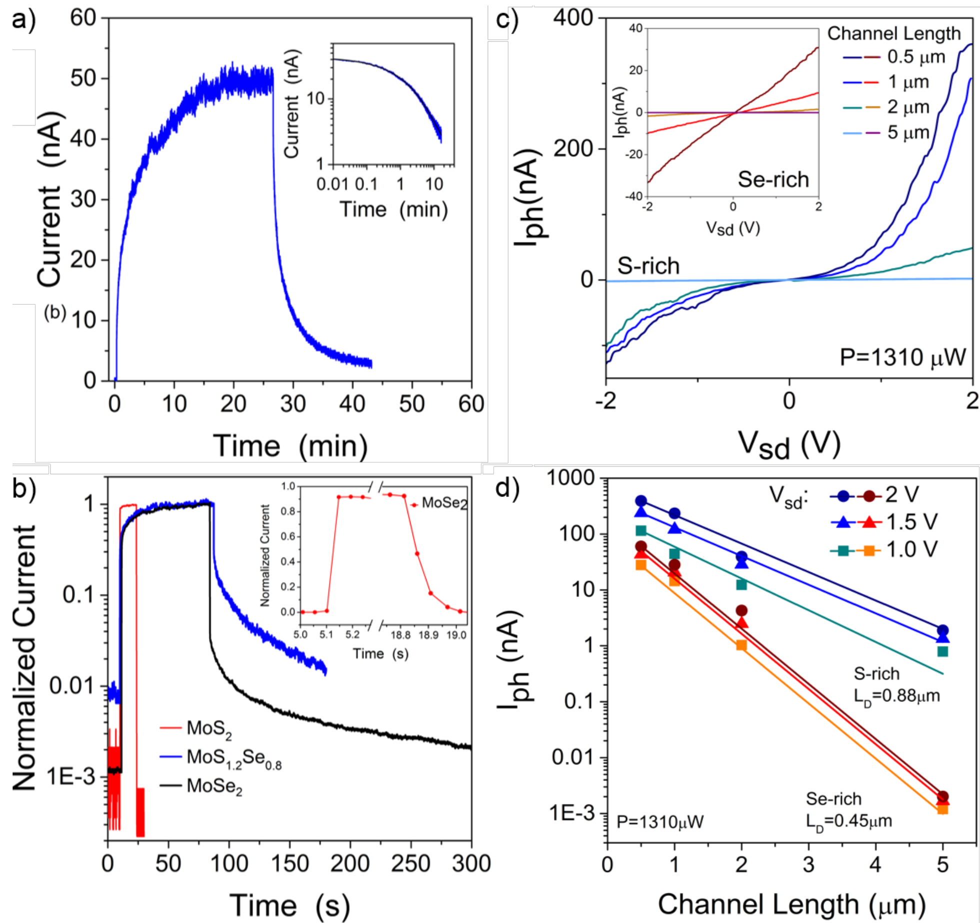

Figure 15. (a) Time-dependence of photocurrent for a MoS_2 device as a laser focused near the drain electrode is turned on and off. The inset shows a fit of the photocurrent decay to a stretched exponential. (b) Comparison of time-dependent response of MoS_2, $MoS_{1.2}Se_{0.8}$ and $MoSe_2$ devices; the inset highlights the fast photocurrent current decrease for a $MoSe_2$ device, which reflects the limit of our electronics. (c) Current-voltage characteristics under illumination (λ=633 nm) for $MoS_{1.8}Se_{0.2}$ and $MoS_{0.4}Se_{1.6}$ (inset) alloy devices of different channel lengths. (d) Dependence of the photocurrent on channel length at 1310μW excitation power.

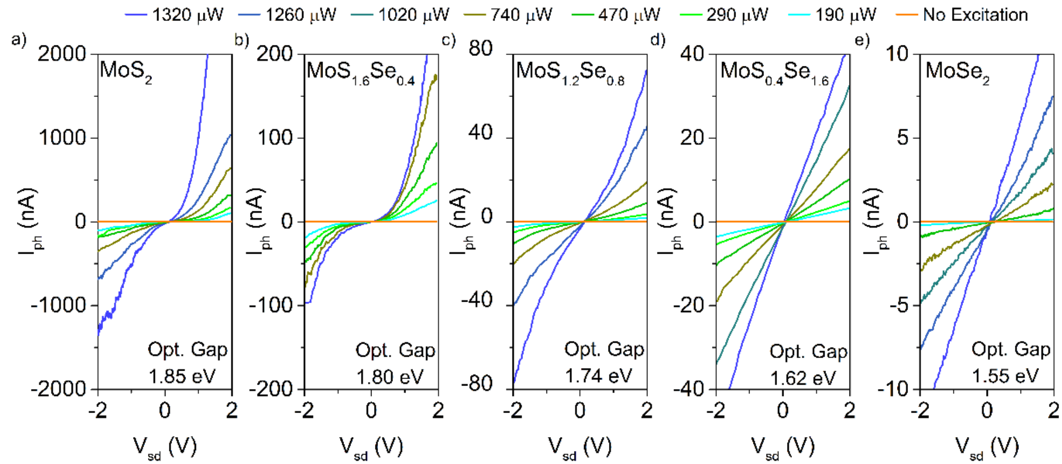

Figure 16. Current-voltage characteristics at different laser powers (λ=633 nm) for five devices ranging in composition from (a) MoS_2 (E_g=1.85 eV) to (e) $MoSe_2$ (E_g=1.55 eV). Laser power labeling is the same for all panels, and all devices have a channel length of 1 μm. The laser position was optimized to give the largest photoresponse at 2V, and kept at that same position as I-V curves were acquired.

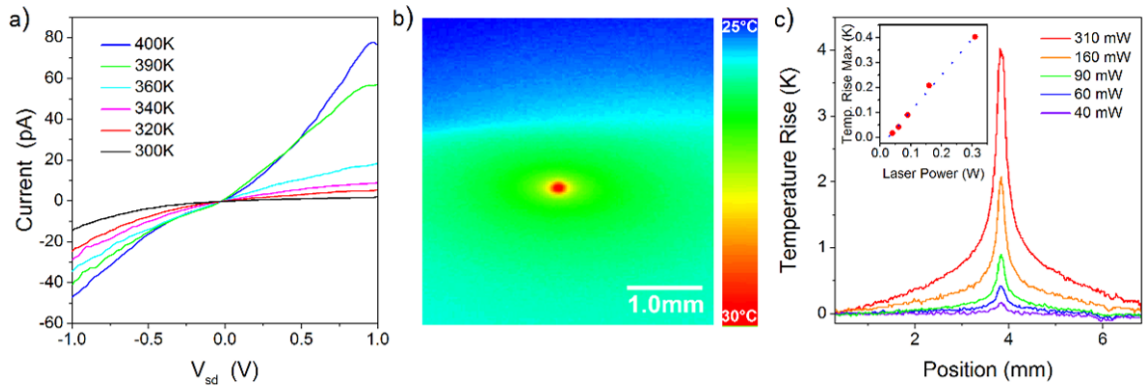

Figure 17. (a) Dark current-voltage characteristics for a 1 micron channel MoS_2 device as a function of temperature. (b) Infrared camera image of a single-layer MoS_2 film on Si/SiO_2 illuminated by a focused red laser at a power of 0.31 W. (c) Profiles of temperature rise extracted from images similar to (b) during laser illumination at different powers. Inset shows the maximum temperature rise as a function of laser power.

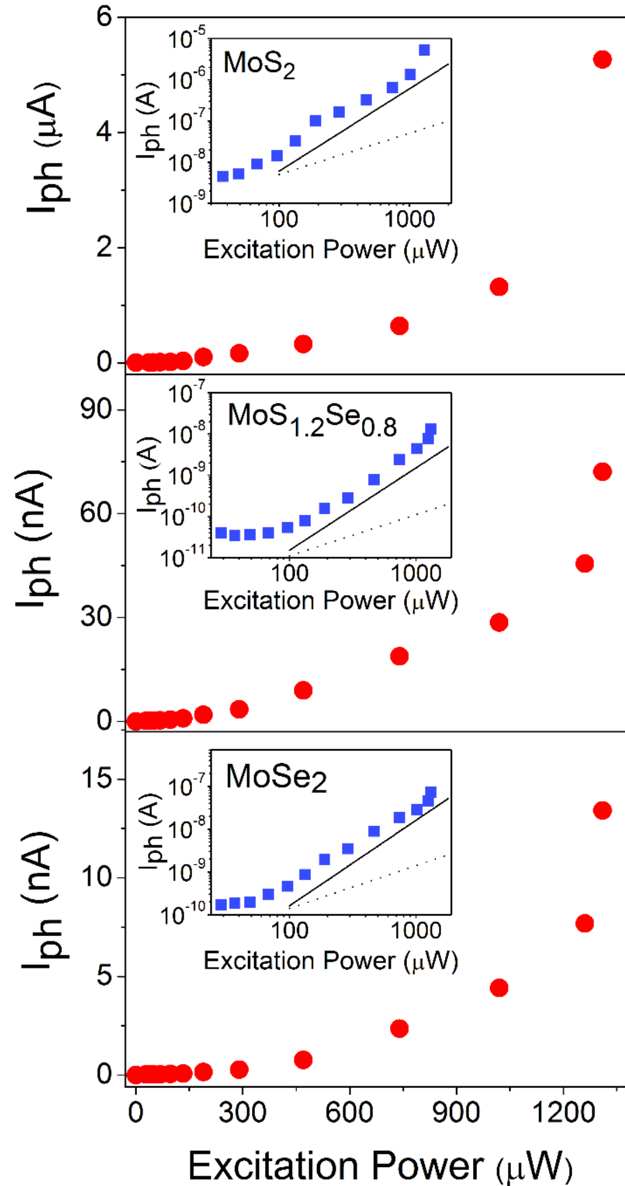

Figure 18. Photocurrent measured at a source-drain bias of 2 V as a function of laser power for single-layer MoS_2 (E_g=1.85 eV), $MoS_{1.2}Se_{0.4}$ (E_g=1.74 eV), and $MoSe_2$ (E_g=1.55 eV). The superlinear behavior is observed across compositions. The insets show log-log plots of the photocurrent as a function of laser power. The solid and dashed lines in the insets correspond to linear and quadratic dependence on power.

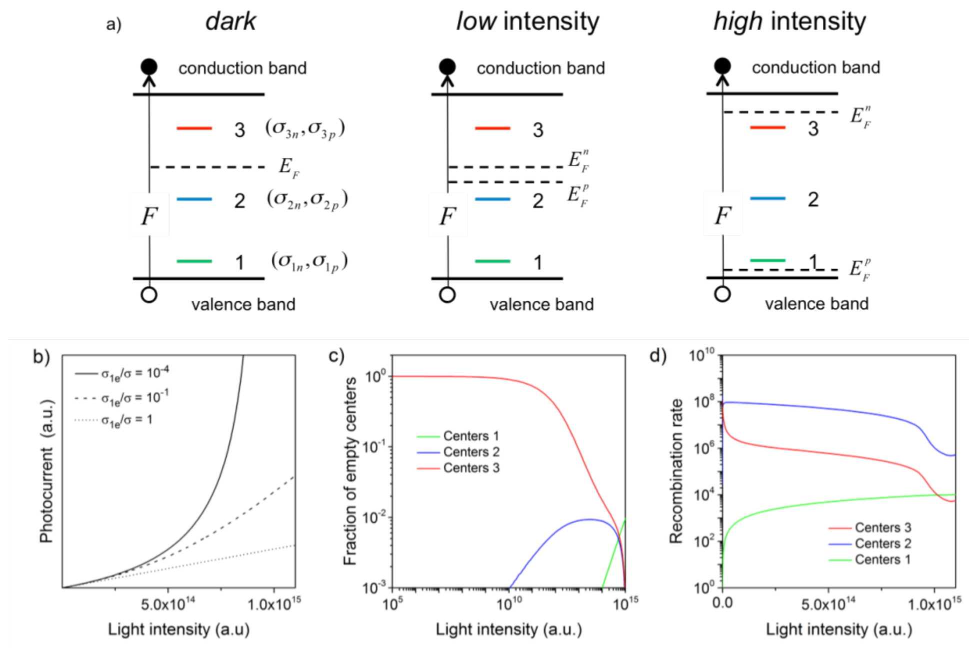

Figure 19. Model to explain the origin of superlinear photocurrent. (a) Illustration of the three different types of recombination centers and their capture cross-sections, as well as the location of the Fermi level in the dark and the quasi Fermi levels under low- and high-intensity illumination. (b) Calculated photocurrent as a function of light intensity for three different values of the ratio of capture cross-sections for centers 1 and 3. (c) Fraction of empty centers as a function of light intensity. (d) Recombination rate as a function of light intensity.

References

(1) Mak, K. F.; Lee, C.; Hone, J.; Shan, J.; Heinz, T. F. Atomically Thin MoS_2: A New Direct-Gap Semiconductor. *Phys. Rev. Lett.* **2010,** *105*, 136805.

(2) Splendiani, A.; Sun, L.; Zhang, Y.; Li, T.; Kim, J.; Chim, C.-Y.; Galli, G.; Wang, F. Emerging Photoluminescence in Monolayer MoS_2. *Nano Lett.* **2010,** *10*, 1271-1275.

(3) Jariwala, D.; Sangwan, V. K.; Lauhon, L. J.; Marks, T. J.; Hersam, M. C. Emerging Device Applications for Semiconducting Two-Dimensional Transition Metal Dichalcogenides. *ACS Nano* **2014,** *8*, 1102-1120.

(4) Mann, J.; Sun, D.; Ma, Q.; Chen, J.-R.; Preciado, E.; Ohta, T.; Diaconescu, B.; Yamaguchi, K.; Tran, T.; Wurch, M.; Magnone, K.; Heinz, T. F.; Kellogg, G. L.; Kawakami, R.; Bartels, L. Facile growth of monolayer MoS_2 film areas on SiO_2. *The European Physical Journal B C7 - 226* **2013,** *86*, 1-4.

(5) Mann, J.; Ma, Q.; Odenthal, P. M.; Isarraraz, M.; Le, D.; Preciado, E.; Barroso, D.; Yamaguchi, K.; von Son Palacio, G.; Nguyen, A.; Tran, T.; Wurch, M.; Nguyen, A.; Klee, V.; Bobek, S.; Sun, D.; Heinz, T. F.; Rahman, T. S.; Kawakami, R.; Bartels, L. 2-Dimensional Transition Metal Dichalcogenides with Tunable Direct Band Gaps: $MoS_{2(1-x)}Se_{2x}$ Monolayers. *Adv. Mater.* **2014,** *26*, 1399-1404.

(6) Feng, Q.; Zhu, Y.; Hong, J.; Zhang, M.; Duan, W.; Mao, N.; Wu, J.; Xu, H.; Dong, F.; Lin, F.; Jin, C.; Wang, C.; Zhang, J.; Xie, L. Growth of Large-Area 2D $MoS_{2(1-x)}Se_{2x}$ Semiconductor Alloys. *Adv. Mater.* **2014,** *26*, 2648-2653.

(7) Yin, Z.; Li, H.; Li, H.; Jiang, L.; Shi, Y.; Sun, Y.; Lu, G.; Zhang, Q.; Chen, X.; Zhang, H. Single-Layer MoS_2 Phototransistors. *ACS Nano* **2011,** *6*, 74-80.

(8) Lopez-Sanchez, O.; Lembke, D.; Kayci, M.; Radenovic, A.; Kis, A. Ultrasensitive photodetectors based on monolayer MoS_2. *Nat Nano* **2013,** *8*, 497-501.

(9) Wu, C.-C.; Jariwala, D.; Sangwan, V. K.; Marks, T. J.; Hersam, M. C.; Lauhon, L. J. Elucidating the Photoresponse of Ultrathin MoS_2 Field-Effect Transistors by Scanning Photocurrent Microscopy. *The Journal of Physical Chemistry Letters* **2013,** *4*, 2508-2513.

(10) Buscema, M.; Barkelid, M.; Zwiller, V.; van der Zant, H. S. J.; Steele, G. A.; Castellanos-Gomez, A. Large and Tunable Photothermoelectric Effect in Single-Layer MoS_2. *Nano Lett.* **2013,** *13*, 358-363.

(11) Perea-López, N.; Lin, Z.; Pradhan, N. R.; Iñiguez-Rábago, A.; Elías, A. L.; McCreary, A.; Lou, J.; Ajayan, P. M.; Terrones, H.; Balicas, L.; Terrones, M. CVD-

grown monolayered MoS_2 as an effective photosensor operating at low-voltage. *2D Materials* **2014,** *1*, 011004.

(12) Komsa, H.-P.; Krasheninnikov, A. V. Two-Dimensional Transition Metal Dichalcogenide Alloys: Stability and Electronic Properties. *The Journal of Physical Chemistry Letters* **2012,** *3*, 3652-3656.

(13) Li, H.; Duan, X.; Wu, X.; Zhuang, X.; Zhou, H.; Zhang, Q.; Zhu, X.; Hu, W.; Ren, P.; Guo, P.; Ma, L.; Fan, X.; Wang, X.; Xu, J.; Pan, A.; Duan, X. Growth of Alloy MoS_{2x}Se2(1−x) Nanosheets with Fully Tunable Chemical Compositions and Optical Properties. *J. Am. Chem. Soc.* **2014,** *136*, 3756-3759.

(14) Dang, X. Z.; Wang, C. D.; Yu, E. T.; Boutros, K. S.; Redwing, J. M. Persistent photoconductivity and defect levels in n-type AlGaN/GaN heterostructures. *Appl. Phys. Lett.* **1998,** *72*, 2745-2747.

(15) Nanot, S.; Cummings, A. W.; Pint, C. L.; Ikeuchi, A.; Akiho, T.; Sueoka, K.; Hauge, R. H.; Léonard, F.; Kono, J. Broadband, Polarization-Sensitive Photodetector Based on Optically-Thick Films of Macroscopically Long, Dense, and Aligned Carbon Nanotubes. *Sci. Rep.* **2013,** *3*, 1335.

(16) Dorgan, V. Ph. D Thesis, University of Illinois at Urbana Champaign, http://hdl.handle.net/2142/49522 **2014**.

(17) Bakr, N. A. Anomalous photoconductive transport properties of As_2Se_3 films. *Egypt. J. Sol.* **2002,** *25*, 13-21.

(18) Unnikrishnan, N. V.; Singh, R. D. Temperature Dependence of Lux-Ampere Characteristicsof CdI_2 Single Crystals. *Phys. Stat. Sol. (a)* **1986,** *96*, K219-K222.

(19) Peters, J. A.; Cho, N. K.; Liu, Z.; Wessels, B. W.; Li, H.; Androulakis, J.; Kanatzidis, M. G. Investigation of defect levels in $Cs_2Hg_6S_7$ single crystals by photoconductivity and photoluminescence spectroscopies. *J. Appl. Phys.* **2012,** *112*, -.

(20) Kushwaha, N.; Kushwaha, V. S.; Kumar, R. K. S. A. Determination of energy of defect centres in a-$Se_{78}Ge_{22}$ thin films. *Phil. Mag. Lett.* **2006,** *86*, 691-697.

(21) Rose, A. Recombination Processes in Insulators and Semiconductors. *Phys. Rev.* **1955,** *97*, 322-333.

(22) Stöckmann, F. Superlinear Photoconductivity. *Phys. Stat. Sol. (b)* **1969,** *34*, 751-757.

(23) Dussel, G. A.; Bube, R. H. Further Considerations on a Theory of Superlinearity in CdS and Related Materials. *J. Appl. Phys.* **1966,** *37*, 13-21.

(24) Zhou, W.; Zou, X.; Najmaei, S.; Liu, Z.; Shi, Y.; Kong, J.; Lou, J.; Ajayan, P. M.; Yakobson, B. I.; Idrobo, J.-C. Intrinsic Structural Defects in Monolayer Molybdenum Disulfide. *Nano Lett.* **2013,** *13*, 2615-2622.

(25) Tongay, S.; Suh, J.; Ataca, C.; Fan, W.; Luce, A.; Kang, J. S.; Liu, J.; Ko, C.; Raghunathanan, R.; Zhou, J.; Ogletree, F.; Li, J.; Grossman, J. C.; Wu, J. Defects activated photoluminescence in two-dimensional semiconductors: interplay between bound, charged, and free excitons. *Sci. Rep.* **2013,** *3*, 2657.

(26) Bollinger, M. V.; Lauritsen, J. V.; Jacobsen, K. W.; Nørskov, J. K.; Helveg, S.; Besenbacher, F. One-Dimensional Metallic Edge States in MoS_2. *Phys. Rev. Lett.* **2001,** *87*, 196803.

(27) Vojvodic, A.; Hinnemann, B.; Nørskov, J. K. Magnetic edge states in MoS_2 characterized using density-functional theory. *Phys. Rev. B* **2009,** *80*, 125416.

(28) Fuhrer, M. S.; Hone, J. Measurement of mobility in dual-gated MoS_2 transistors. *Nat Nano* **2013,** *8*, 146-147.

Chapter 4

Toward Ferroelectric Control of Monolayer MoS_2

The following is taken from an article published in Nano Letters [REF] and is presented here with kind permission of Nano Letters (NANO LETT) and American Chemical Society Publications (ACS). This collaborative work was performed by me and the following students and collaborators.

Ariana Nguyen[1], Pankaj Sharma[2], Thomas Scott[2], Edwin Preciado[1], Velveth Klee[1], Dezheng Sun[3], I-Hsi (Daniel) Lu[1], David Barroso[1], SukHyun Kim[3], Vladimir Ya. Shur[4], Andrey R. Akhmatkhanov[4], Alexei Gruverman[2], Ludwig Bartels[1] and Peter A. Dowben[2]

[1]Chemistry and Materials Science & Engineering Program, University of California, Riverside, CA 92521, USA

[2]Department of Physics and Astronomy, Theodore Jorgensen Hall, 855 North 16th Street, University of Nebraska-Lincoln, Lincoln, NE 68588-0299, USA

[3]Columbia University, 3000 Broadway, New York, NY 10027-6941, USA

[4]Institute of Natural Sciences, Ural Federal University, Ekaterinburg, 620000, Russia

Introduction

Transition metal dichalcogenides MX_2 (with M = Mo, W and X = S, Se, Te) monolayers have been fabricated into nanoscale transistors [1-8] that by electrostatic gating achieve high on-off ratios not shared by the gapless semiconductor graphene. Ferroelectric gating, similar to what has been reported in graphene-based [9-12] and MoS_2 based [13] field effect transistors on various ferroelectrics, are a potential route towards low power, nonvolatile two-dimensional (2D) metal dichalcogenide conduction channel transistors. For the development of such a nonvolatile ferroelectric gated

transistor to have true impact, the fabrication should be scalable – this means fabrication not by transfer of the 2D film, but rather by growth “in place” that translate to large-scale manufacturing. One such approach is chemical vapor deposition (CVD) of the 2D conduction channel material directly onto the ferroelectric, but the growth must preserve ferroelectricity and the ability to retain a dipole as well as an interface charge. These are not small challenges as under ambient conditions surface dipoles/interface charges are typically compensated by accumulation of ionic/dipolar species or through redistribution of mobile carriers in the bulk [14]. This screening significantly affects the surface charge distribution/potential and additionally can result in band bending [15].

Materials and Methods

Here, we demonstrate the growth of high-quality single-layer MoS_2 films directly onto periodically poled $LiNbO_3$ (PPLN) substrates. We find a significant effect of the ferroelectric polarization on the growth and transport properties of the MoS_2 films. The choice of lithium niobate ($LiNbO_3$) as a ferroelectric substrate for this study was motivated by the fact that lithium niobate exhibits a ferroelectric transition temperature well above 1000° C, thus preserving the ferroelectric domain structure during the deposition of the MoS_2 film at a temperature of ~ 700° C [16]. Our lithium niobate substrates were cut perpendicular to the c (polar) axis resulting in a surface of hexagonal symmetry and perpendicular polarization domains.

Chemical vapor deposition (CVD) growth of single-layer MoS_2 [17-21] has been demonstrated on SiO_2 and a few other substrates. The resultant films exhibit optical and transport properties that rival those of mechanically exfoliated films. Single-layer MoS_2, exfoliated or grown on SiO_2/Si, typically shows characteristic n-doped transport [5,6,22-23]. In most cases, an inversion of the MoS_2 transport properties to p-type behavior, say through application of a sufficiently strong electrical field, has not been shown feasible except by the use of special materials such as ionic liquids [2,24]. MoS_2 on lithium niobate appears to be different.

Complete fabrication and characterization details are given in the SI. Briefly, as substrates we used 5 x 5 x 0.5 mm^3 plane-parallel plates of lithium niobate of congruent composition, with a periodic domain pattern (period of 12~16 μm) made by several approaches. The periodic domain pattern was, in the majority of the samples, prepared by 10 kV voltage application to 3-inch $LiNbO_3$ wafer (0.5 mm thick) using liquid electrodes of saturated aqueous LiCl [25,26]. The *c*+ polar (Z+) surface was covered by a lithographic photoresist pattern whereas the *c*- polar (Z-) surface was contacted by a continuous liquid electrode, and the photoresist pattern was removed after the poling process by dimethyl sulfoxide and oxygen-plasma dry etching, leaving behind a bare ferroelectric surface. As a result, the lithium niobate substrates exhibit periodic domain stripes of antiparallel 180° ferroelectric domains with spontaneous polarization, oriented either upward or downward along the surface normal. The characteristic dimensions of the domain patterns were measured in ambient environment by means of piezoresponse force microscopy (PFM) [27-31]. The various approaches to the fabrication of the

periodic domain pattern were seen to affect the surface morphology, but without any other significant difference in the results reported here. For the transport measurements, we deposited Ti/Au electrical contacts for transport measurements on the MoS_2 single-layer film using electron-beam lithography and a MMA/PMMA stack as a resist. Our process is optimized to be benign to the MoS_2 overlayer, as validated by the absence of significant degradation of the photoluminescence yield.

MoS_2(0001) monolayer thin film growth, on the periodically poled lithium niobate, proceeded as described in Ref. [21]. We used alumina boats containing elemental sulfur and MoO_3 powder as sources of sulfur and molybdenum, respectively. The boats were placed at different positions in a quartz process tube and inserted into a tube furnace. The comparatively small substrate was supported by means of a molybdenum mesh on the edge of the MoO_3-containing alumina boat. The sulfur vapor from the upstream sulfur boat passed over the sample, aided by an N_2 carrier gas. Heating of the furnace to 650-700° C at the MoO_3 boat position and slow cool-down yielded films with a range of MoS_2 coverages from single-layer films to isolated MoS_2 islands, depending on the growth temperature and duration. The growth MoS_2 overlayers, up to single-layer films under our conditions, was seen to preserve the ferroelectric domain pattern of $LiNbO_3$ substrate.

Results

We found enhanced MoS_2 growth on the domains with polarization oriented "up" compared to domains with polarization oriented "down". At low coverages of MoS_2 deposition, we find the majority of the resultant MoS_2 islands on up-domains of the periodically poled $LiNbO_3$ substrate. More deposition led to the formation of a continuous MoS_2 film on both up- and down-domains. Under some intermediate deposition conditions, we observed an almost continuous film on the up-domains and practically no film growth on the down domains, as illustrated in Figure 1 (up-domains). Figure 20a shows an optical micrograph of an area where the MoS_2 single-layer film (directly visible as brighter areas) follows the periodic polarization domain pattern of the $LiNbO_3$ substrate (indicated at the bottom of Figure 20a): areas with the substrate dipole moment pointing up out of the surface (up-domains) exhibit MoS_2 growth, while areas with down polarization (down-domains) support less or no growth.

The preferential growth of MoS_2 on the up-domains and absence on the down-domains is validated by mapping of the photoluminescence (PL) intensity of the A exciton at 1.86 eV photon energy (Figure 20b). The photoluminescence spectra obtained at 100 K on the MoS_2 areas (Figure 20c) show the well known A and B exciton peaks, confirming the growth of quality MoS_2(0001) single-layer materials on this substrate. Because MoS_2 is a direct bandgap semiconductor exclusively at the single-layer limit [32-34], the presence of bilayer or thicker films would result in a significantly reduced

and spectrally shifted photoluminescence signal [34]. The strong overlap between MoS_2 and $LiNbO_3$ vibrational modes makes Raman spectroscopy less useful.

While not previously reported for any 2D material, the preferential growth of MoS_2 on ferroelectric domains of a particular polarization has considerable precedence. Enhanced adsorption on one polarization domain of a ferroelectric over the opposite polarization has been reported previously [31,35-43] for small molecules, viruses, and metals. The electrically switchable properties of the ferroelectrics can be used to tailor surface reactivity, yet the physico-chemical mechanism of preferred adsorption on one polar surface is not conclusively understood. Inspection of the details of the surface composition of $LiNbO_3$ as a function of temperature [44] indicates that the surface stoichiometry and arrangement of this material differs with polarization under our growth conditions/temperature. At elevated temperatures, as during MoS_2 CVD growth, far greater evaporation of Li and especially oxygen has been observed from the up-domains than from the down-domains [44], and thus should facilitate reduction of any ambient compensating charges. This could enhance the existence of free Nb or lithium frontier orbitals and an oxygen poor surface terminal layer for the up-domain compared to a down-domain [45,46]. In the computational studies of poled $LiNbO_3$ surfaces by both Levchenko and Rappe [45] and Sanna *et al*. [46] the up-domains exhibit less oxygen atoms at the terminal surface layer compared to the down-domain surface thereby facilitating the adsorption/anchoring and reduction of MoO_3 during CVD growth. Preferential growth, on one domain over the other, is be mediated by surface chemistry, as has been speculated upon elsewhere [41]. In the case of the preferred MoS_2 growth on

the up-domain surface, this is likely facilitated by the adsorption/anchoring and reduction of attachment of MoO_{3-x}, thereby seeding MoS_2 and leading to preferential growth on this domain. Such terminal layer site occupation [45,46] occurs in spite of the overall oxygen and lithium rich surface region of the up-domains compared to the negative or down-domain ferroelectric surface, as noted in both experiment [44] and the theory of Levchenko and Rappe [45] and Sanna *et al*. [46]. We caution that the surfaces of ferroelectrics are complicated and a detailed analysis of the surface composition, under MoS_2 growth conditions, is experimentally well beyond the scope of this study.

We utilized piezoresponse force microscopy [27-31] to image ferroelectric domains on $LiNbO_3$ substrates, as seen in Figure 21 and the SI. This method exploits as contrast mechanism the fact that ferroelectric behavior implies piezoelectricity. Consequently, mapping the piezoelectric response of a material provides a direct image of its ferroelectric domain structure. We find that MoS_2 monolayers preserve the surface dipoles, as seen in Figure 21. Piezoresponse force microscopy (PFM) and Kelvin probe force microscopy (KPFM) were conducted on a sample exhibiting isolated MoS_2 islands, i.e. a reduced CVD coverage compared to that of Figure 20, with growth on the up- and, to a lesser degree on the down-domains. At such MoS_2 coverages, we observe that the MoS_2 islands on the up-domain frequently touch the substrate domain boundary but generally do not span across the ferroelectric domain boundary into the adjacent ferroelectric polarization domains. The PFM phase image (Figure 21b) indicates the perodic ferroelectric domain stripes (here, darker contrast corresponds to up-domains and brighter contrast indicates down-domains). The PFM amplitude image (Figure 21a) of the

same area shows MoS_2 islands on ferroelectric up-domains as bright features meaning that the absolute value of the electric field, which generates the PFM signal at the $MoS_2/LiNbO_3$ interface, is greater here than elsewhere. While ambient conditions generally lead to a suppression of the surface polarization charge, this effect is mitigated where the MoS_2 islands cover the up-domains, similar to prior experiments on graphene [9,10]. In contrast, the PFM amplitude is reduced over the MoS_2 islands on the down-domains. We can reconcile these two findings by invoking a chemically-induced charge transfer from MoS_2 to the $LiNbO_3$ substrate whose direction (but not magnitude) is irrespective of the substrate polarization, i.e. MoS_2 donates electron charge to both the oxygen rich up domain surface and the down domain surface.

Corroborating evidence of the induced $MoS_2/LiNbO_3$ charge transfer and ensuing dipole interactions originates from Kelvin probe force microscopy (KPFM) data (Figure 2c,d) [47]. The KPFM image of Figure 21c shows two adjacent opposite (180º) ferroelectric polarization domains, with the ferroelectric domain boundary running almost vertically through the image. In each domain, isolated MoS_2 islands appear as reduction of the surface potential (i.e. increase of the work function) irrespective of the surface polarization direction. The cross-sectional profile of the relative surface potential, shown in Figure 21d, reveals a reduction by ~50 mV over the MoS_2 islands. This local reduction in surface potential is consistent with the direction of a surface dipole that originates from electron transfer from the MoS_2 islands to the substrate, as suggested by the PFM results of Figure 21a,b.

We note that the chemically induced dipole of the MoS_2 on $LiNbO_3$ (independent of polarization direction) indicates sizeable interaction across the interface. Yet the remnant surface polarization under the MoS_2 film offers the possibility for affecting the overlayer transport properties through substrate polarization.

We performed electrical transport measurements (Figure 22) on up-domains (positive boundary charge) and down-domains (negative boundary charge). To this end, we fabricated Ti/Au contacts onto a continuous MoS_2 film spanning both substrate polarities. The transport was measured for a channel length between the contacts of 1 μm aligned with the domain stripes (vertical in Figure 22b). The photoluminescence spectra of Figure 20d were obtained on these ferroelectric domain stripes prior to contact fabrication, with the red/blue spectrum corresponding to the electrode pair marked in the same color in Figure 22b.

The current-voltage-measurements were conducted over a source-drain bias (V_{sd}) range of ±1 V resulting in currents (I_{sd}) in the sub-nanoampere range consistent with typical measurements of MoS_2 in the dark and in the absence of means for alleviating the impact of Schottky barriers [17]. We applied an additional voltage (V_{pol}) of up to ±200 V by means of placing the $LiNbO_3$ substrate on top of a biased metal plate. This is far less than the coercive voltage of the ferroelectric domains, so no domain reversal occurred and no hysteresis was observed. Figure 22a shows the source-drain currents, I_{sd}, for the MoS_2 on both up- and down-domains (measured at V_{sd} = -1 V) as a function of V_{pol}. The displayed currents, I_{sd}, were corrected for leakage caused by the finite resistance of our substrate. The supporting information shows the raw data.

The remanent surface polarization of the ferroelectric $LiNbO_3$ substrate, under the continuous MoS_2 film, offers opportunities for affecting the transport properties of the overlayer. Application of a negative V_{pol}, along the polarization axis, causes the $LiNbO_3$ substrate to accumulate positive charge at its bottom surface and a negative interface charge at the top surface where the MoS_2 film resides (schematic diagrams at the top of Figure 22). For an up-domain, this reduces the positive boundary charge and, thus, reduces electron transfer from the MoS_2 to the substrate. On a down-domain, the applied negative V_{pol} amplifies the negative boundary charge present from the ferroelectric polarization. This attenuates the electron transfer out of the MoS_2 film, indicated by the KPFM measurements. For either substrate polarization domain, i.e. either ferroelectric domain orientation, the application of a negative V_{pol} voltage increases the electron density remaining in the MoS_2 and, hence, is likely to enhance the intrinsic n-doped character. This differs significantly from capacitive gating of a device, while capacitive effects on the channel are minimized by the thickness of the substrate compared to the channel length.

The results of Figure 22 reflect the native n-type character of single-layer MoS_2. With increasing magnitude of negative V_{pol} we observe higher currents, I_{sd}, which is attributed to enhanced n-type carrier concentrations in the MoS_2 single-layer conduction channel (left side of Figure 22a). The result is that higher overall conductivities are reached on the down-domain (blue), where a negative boundary charge supports higher electron density in the MoS_2 film in the first place. In contrast, on an up-domain, the positive substrate boundary charge counters the effect of the applied V_{pol} voltage and

reduces overall electron density in the MoS_2 film, similar to transistors fabricated with an organic semiconductor on a ferroelectric [48].

More interesting is the application of positive V_{pol} (right side of Figure 22a), which leads to an increase in positive charge at the top ferroelectric surface, and in turn amplifies the electron transfer from the MoS_2 film to the $LiNbO_3$, induced by the $MoS_2/LiNbO_3$ interaction. As the MoS_2 appears intrinsically n-doped, this reduces the number of its n-type carriers and, hence, reduces the source-drain current I_{sd}. For the case of a down-domain, a positive V_{pol} is partially compensated by the domain polarization. Consequently, we find that positive V_{pol} has little effect on the electrical transport of MoS_2 on the down-domain. However, transport between the electrode pair on the up-domain (red) goes through a minimum as V_{pol} reaches ~80 V and steeply increases for higher V_{pol}. This reflects inversion of the transport character of the MoS_2 film from n-type to p-type caused by the combination of polarization-independent electron transfer from MoS_2 to $LiNbO_3$ and the surface charge at the $LiNbO_3$ positive domain interface, which is amplified by application of V_{pol}.

The change of the MoS_2 film conductivity by means of substrate polarization and applied voltage is readily reversible and we observed differences in I_{sd} for up- and down-domains by a factor of >2 for a range of static gate voltages. The 2 μm width contacts, aligned with the domain stripes, are sufficiently narrow to restrict MoS_2 transport to material on only one polarization domain, as validated by measurements of the conductance (diagonally) between electrodes on the up- and down-domains.

While for technological application a substantial (i.e., larger than ×2) difference between the transport over up- and down-domains in the absence of an applied voltage is desirable, we wish to point out that in a future nonvolatile transistor based on reversible ferroelectric polarization of the substrate under the MoS_2 channel, the ferroelectric interaction and not the applied "gate" voltages V_{pol} takes the role of the gate. Moreover, variation of the composition of the transition metal dichalcogenide and the ferroelectric substrate may lead to a material combination that requires a V_{pol} only for changing the polarization of the ferroelectric material (write operation) but not for transistor conductance (read operation). Nonvolatile gating by reversible ferroelectric polarization has been observed for p-type organic semiconductors on ferroelectrics [48-54]; and MoS_2 top gated by the organic ferroelectric polyvinylidene fluoride with trifluoroethylene (PVDF-TrFE) [13]. The combination of a ferroelectric gate with a suitable metal dichalcogenides could lead to nonvolatile transistors with appreciably higher mobilities; mobilities as high as 220 $cm^2/(V{\cdot}s)$, with on/off ratios of up to 10^5 were shown by Lee and coworkers for exfoliated MoS_2 [13].

Our transfer-free approach to ferroelectric gated MoS_2 transistors utilizes exclusively scalable processing techniques and, hence, has the potential serve as the foundation for large scale device development. In this context we note, that while the coercive voltage in this study is high, much smaller ones are obtained for thin film ferroelectrics [13,48,55]. Also submicron ferroelectric domains in $LiNbO_3$ are known [27-29], so that much smaller ferroelectric domain pattering of MoS_2 device structures are certainly within the realms of the possible. We hope that our observations will spark

consideration of transition metal dichalcogenide films on switchable ferroelectric substrate as active elements in future nonvolatile microelectronic architectures.

Figures

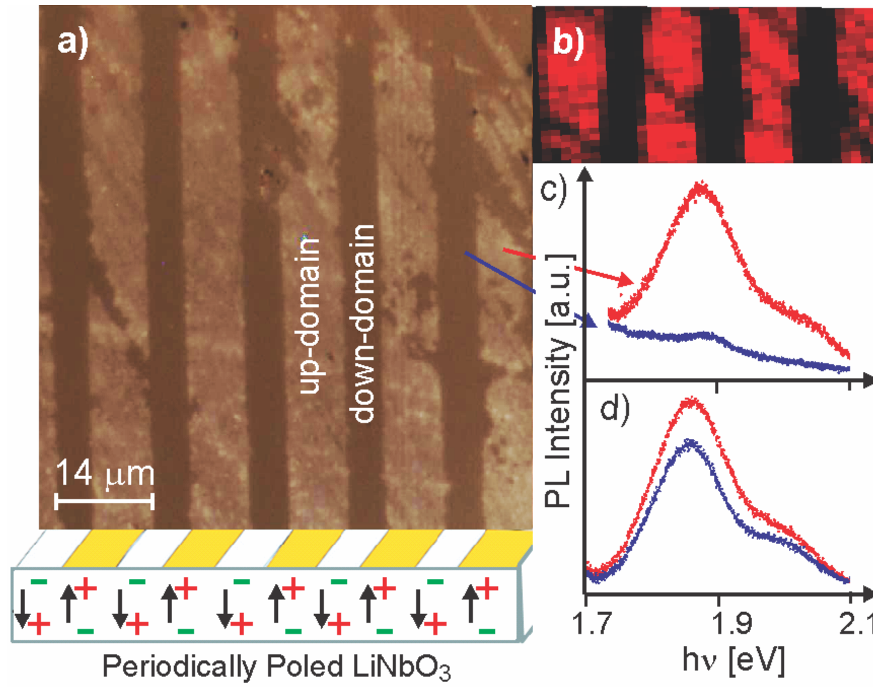

Figure 20. a) The optical micrograph shows preferential growth of single-layer MoS_2 on $LiNbO_3$ domains with a dipole moment pointing up out of the surface, as illustrated in the bottom; (b) spatial mapping of the photoluminescence (PL) intensity (red) of a portion of panel a (same length scale) on the left and (c) spectroscopy validates the single-layer character and quality of the MoS_2 single layer film. When a continuous MoS_2 film is grown on both ferroelectric domains, only a small difference of the PL yield results (d).

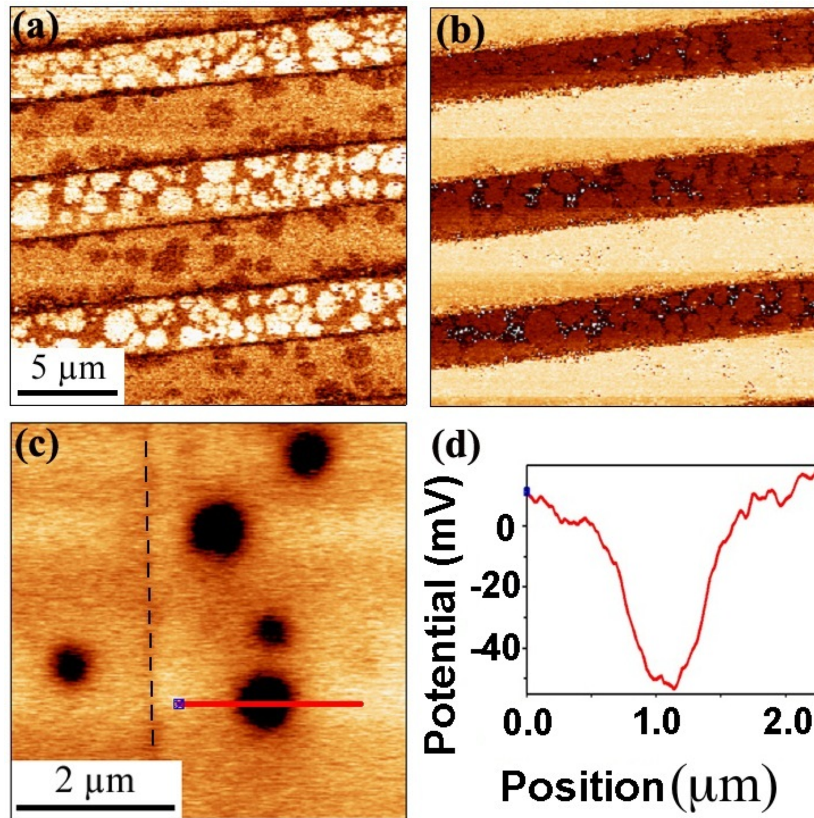

Figure 21. The PFM amplitude (a) and phase (b) images of the same area of the PPLN substrate covered with isolated single-layer MoS_2 islands. Bright and dark contrast in (b) indicates down- and up-domains, respectively. In (a), the MoS_2 islands enhance the amplitude of the piezoresponse signal on the up-domains but suppress the force on the down-domains. (c) Kelvin probe force microscopy (KPFM) reveals a change in surface potential, by about 48-52 mV, at the location of single-layer MoS_2 islands (dark spots) irrespective of the substrate polarization. The dashed line indicates a ferroelectric domain boundary. d) The cross-sectional profile taken along the red line in (c) indicates a change in surface potential across a MoS_2 island.

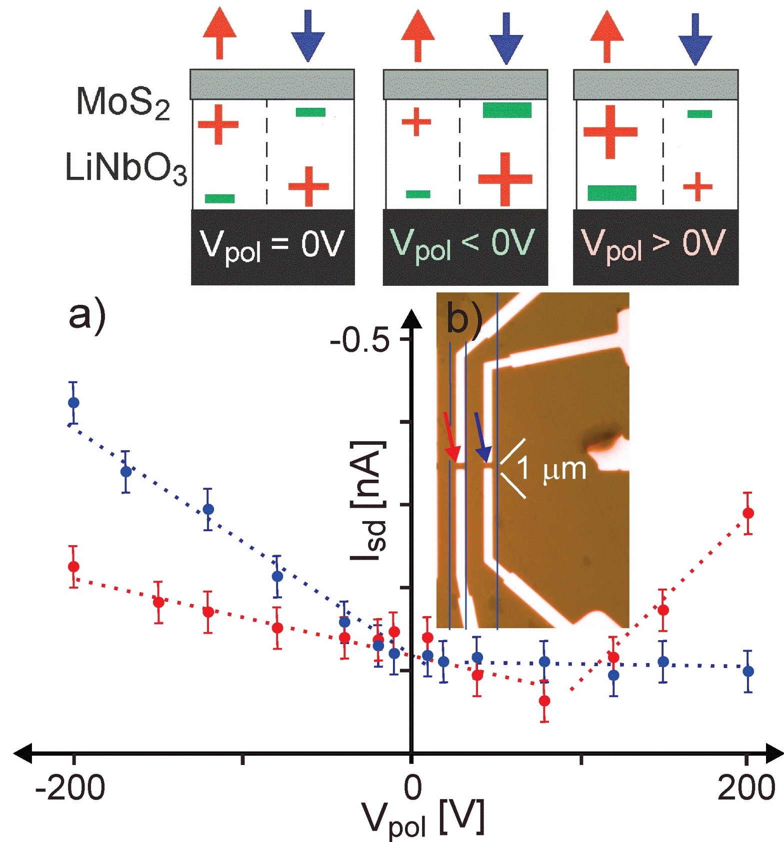

Figure 22. (a) Dependence of the corrected source-drain current I_{sd} on an additional voltage V_{pol} applied to the bottom of the ferroelectric substrate. The red and blue traces correspond to measurement across the 1 μm gaps indicated in panel (b). The approximate location of the domain boundaries are denoted by blue lines. While the left (red) device shows moderate response to negative applied voltage (corresponding to extrinsic n-doping), it can be inverted for positive V_{pol} (extrinsic hole doping) at ~80 V; in contrast the right (blue) device shows higher current under negative V_{pol} but cannot be inverted effectively below V_{pol} = 200 V. The dashed lines are meant to guide the eye. The diagrams schematically illustrate the effect of the applied V_{pol} voltage to the bottom of the ferroelectric $LiNbO_3$ substrate: the left (up) polarization domain corresponds to the left (red) device and vice versa.

References

1. Liu, H.; Si, M.; Deng, Y.; Neal, A. T.; Du, Y.; Najmaei, S.; Ajayan, P. M.; Lou, J.; Ye, P. D. *ACS Nano* **2014,** *8*, 1031-1038.

2. Chuang, S.; Battaglia, C.; Azcatl, A.; McDonnell, S.; Kang, J. S.; Yin, X.; Tosun, M.; Kapadia, R.; Fang, H.; Wallace, R. M.; Javey, A. *Nano Letters* **2014,** *14*, 1337-1342.

3. Chen, J.-R.; Odenthal, P. M.; Swartz, A. G.; Floyd, G. C.; Wen, H.; Luo, K. Y.; Kawakami, R. K. *Nano Letters* **2013,** *13*, 3106-3110.

4. Choi, M. S.; Lee, G.-H.; Yu, Y.-J.; Lee, D.-Y.; Hwan Lee, S.; Kim, P.; Hone, J.; Jong Yoo, W. *Nat. Commun* **2013,** *4*, 1624.

5. Kappera, R.; Voiry, D.; Yalcin, S. E.; Branch, B.; Gupta, G.; Mohite, A. D.; Chowalla, M. *Nat. Mater* **2014,** *13*, 1128-1134.

6. Radisavljevic, B.; Radenovic A.; Brivio J.; Giacometti V.; Kis A., Single-layer MoS_2 transistors. *Nat. Nano* **2011,** *6*, 147-150.

7. Chang, H.-Y.; Zhu, W.; Akinwande, D. *Applied Physics Letters* **2014,** *104*, 113504-113504-5.

8. Tosun, M.; Chuang, S.; Fang, H.; Sachid, A. B.; Hettick, M.; Lin, Y.; Zeng, Y.; Javey, A. *ACS Nano* **2014,** *8*, 4948-4953.

9. Hong, X.; Hoffman, J.; Posadas, A.; Zou, K.; Ahn, C. H.; Zhu, J. *Applied Physics Letters* **2010,** *97*, 033114.

10. Hong, X.; Zou, K.; DaSilva, A. M.; Ahn, C. H.; Zhu, J. *Solid State Communications* **2012,** *152* (15), 1365-1374.

11. Zheng, Y.; Ni, G.-X.; Toh, C.-T.; Zeng, M.-G.; Chen, S.-T.; Yao, K.; Özyilmaz, B. *Applied Physics Letters* **2009,** *94*, 163505.

12. Hong, X.; Posadas, A.; Zou, K.; Ahn, C. H.; Zhu, J. *Physical Review Letters* **2009,** *102*, 136808.

13. Lee, H. S.; Min, S.-W.; Park, M. K.; Lee, Y. T.; Jeon, P. J.; Kim, J. H.; Ryu, S.; Im, S. *Small* **2012,** *8*, 3111-3115.

14. Fridkin, V. M., V. M. Fridkin: Ferroelectric Semiconductors. Consultants Bureau, a Division of Plenum Publishing Corporation, New York. **1980,** *15*, 1392-1392.

15. Yang, W.-C.; Rodriguez, B. J.; Gruverman, A.; Nemanich, R. J. *Applied Physics Letters* **2004,** *85* (12), 2316-2318.

16. Smolenskii, G. A.; Krainik, N. N.; Khuchua, N. P.; Zhdanova, V. V.; Mylnikova, I. E. *Physica Status Solidi (b)* **1966,** *13*, 309-314.

17. van der Zande, A. M.; Huang, P. Y.; Chenet, D. A.; Berkelbach, T. C.; You, Y.; Lee, G.-H.; Heinz, T. F.; Reichman, D. R.; Muller, D. A.; Hone, J. C. *Nat. Mater* **2013,** *12*, 554-561.

18. Yu, Y.; Li, C.; Liu, Y.; Su, L.; Zhang, Y.; Cao, L. *Sci. Rep.* **2013,** *3*,1866.

19. Zhan, Y.; Liu, Z.; Najmaei, S.; Ajayan, P. M.; Lou, J. *Small* **2012,** *8*, 966-971.

20. McCreary, K. M.; Hanbicki, A. T.; Robinson, J. T.; Cobas, E.; Culbertson, J. C.; Friedman, A. L.; Jernigan, G. G.; Jonker, B. T. *Advanced Functional Materials* **2014,** *24*, 6449-6454.

21. Mann, J.; Sun, D.; Ma, Q.; Chen, J.-R.; Preciado, E.; Ohta, T.; Diaconescu, B.; Yamaguchi, K.; Tran, T.; Wurch, M.; Magnone, K.; Heinz, T. F.; Kellogg, G. L.; Kawakami, R.; Bartels, L. *The European Physical Journal B* **2013,** *86*, 1-4.

22. Wang, L.; Meric, I.; Huang, P. Y.; Gao, Q.; Gao, Y.; Tran, H.; Taniguchi, T.; Watanabe, K.; Campos, L. M.; Muller, D. A.; Guo, J.; Kim, P.; Hone, J.; Shepard, K. L.; Dean, C. R. *Science* **2013,** *342*, 614-617.

23. Baugher, B. W. H.; Churchill, H. O. H.; Yang, Y.; Jarillo-Herrero, P. *Nano Letters* **2013,** *13*, 4212-4216.

24. Zhang, Y.; Ye, J.; Matsuhashi, Y.; Iwasa, Y. *Nano Letters* **2012,** *12*, 1136-1140.

25. Shur, V. Y.; Rumyantsev, E. L.; Nikolaeva, E. V.; Shishkin, E. I.; Fursov, D. V.; Batchko, R. G.; Eyres, L. A.; Fejer, M. M.; Byer, R. L. *Applied Physics Letters* **2000,** *76*, 143-145.

26. Shur, V. Y.; Rumyantsev, E. L.; Nikolaeva, E. V.; Shishkin, E. I.; Batchko, R. G.; Miller, G. D.; Fejer, M. M.; Byer, R. L. *Ferroelectrics* **2000,** *236*, 129-144.

27. Rodriguez, B. J.; Nemanich, R. J.; Kingon, A.; Gruverman, A.; Kalinin, S. V.; Terabe, K.; Liu, X. Y.; Kitamura, K. *Applied Physics Letters* **2005,** *86*, 012906.

28. Gruverman, A.; Kalinin, S. V. *Journal of Materials Science* **2006,** *41*, 107-116.

29. Gruverman, A.; Auciello, O.; Tokumoto, H. *Annual Review of Materials Science* **1998,** *28*, 101-123.

30. Gruverman, A.; Auciello, O.; Hatano, J.; Tokumoto, H. *Ferroelectrics* **1996,** *184*, 11-20.

31. Kalinin, S. V.; Bonnell, D. A.; Alvarez, T.; Lei, X.; Hu, Z.; Ferris, J. H.; Zhang, Q.; Dunn, S. *Nano Letters* **2002,** *2*, 589-593.

32. Yun, W. S.; Han, S. W.; Hong, S. C.; Kim, I. G.; Lee, J. D. *Physical Review B* **2012,** *85*, 033305.

33. Jin, W.; Yeh, P.-C.; Zaki, N.; Zhang, D.; Sadowski, J. T.; Al-Mahboob, A.; van der Zande, A. M.; Chenet, D. A.; Dadap, J. I.; Herman, I. P.; Sutter, P.; Hone, J.; Osgood, R. M. *Physical Review Letters* **2013,** *111*, 106801.

34. Mak, K. F.; Lee, C.; Hone, J.; Shan, J.; Heinz, T. F. *Physical Review Letters* **2010,** *105* (13), 136805.

35. Inoue, Y.; Sato, K.; Suzuki, S. *Journal of Physical Chemistry* **1985,** *89*, 2827-2831.

36. Dunn, S.; Jones, P. M.; Gallardo, D. E. *Journal of the American Chemical Society* **2007,** *129*, 8724-8728.

37. Liu, X.; Kitamura, K.; Terabe, K.; Hatano, H.; Ohashi, N. *Applied Physics Letters* **2007,** *91*, 044101.

38. Dunn, S.; Cullen, D.; Abad-Garcia, E.; Bertoni, C.; Carter, R.; Howorth, D.; Whatmore, R. W. *Applied Physics Letters* **2004,** *85*, 3537-3539.

39. Kim, S.; Schoenberg, M. R.; Rappe, A. M. *Physical Review Letters* **2011,** *107*, 076102.

40. Zhang, Z.; Sharma, P.; Borca, C. N.; Dowben, P. A.; Gruverman, A. *Applied Physics Letters* **2010,** *97*, 243702.

41. Xiao, J.; Zhang, Z.; Wu, D.; Routaboul, L.; Braunstein, P.; Doudin, B.; Losovyj, Y. B.; Kizilkaya, O.; Rosa, L. G.; Borca, C. N.; Gruverman, A.; Dowben, P. A. *Physical Chemistry Chemical Physics* **2010,** *12*, 10329-10340.

42. Yun, Y.; Altman, E. I. *J. American Chemical Society* **2007,** *129*, 15684-15689.

43. Garra, J.; Vohs, J. M.; Bonnell, D. A. *Surface Science* **2009,** *603*, 1106-1114.

44. Lushkin, A. Ye., Nazarenko, V. B., Pilipchack, K. N., Shnyukov, V. F.; Naumovets, A. G. *Journal of Physics D: Applied Physics* **1999,** 32, 22-28.

45. Levchenko, S. V.; Rappe, A. M. *Physical Review Letters* **2008,** *100*, 256101.

46. Sanna, S.; Gavrilenko, A. V.; Schmidt, W. G. *Physica Status Solidi (c)* **2010,** *7*, 145-148.

47. Melitz, W.; Shen, J.; Kummel, A. C.; Lee, S. *Surface Science Reports* **2011,** *66*, 1-27.

48. Dowben, P. A.; Rosa, L. G.; Ilie C.C.; Xiao, J. *Journal of Electron Spectroscopy and Related Phenomena* **2009**, *174*, 10-21.

49. Naber, R. C. G.; Tanase, C.; Blom, P. W. M.; Gelinck, G. H.; Marsman, A. W.; Touwslager, F. J.; Setayesh, S.; de Leeuw, D. M. *Nat. Mater* **2005,** *4*, 243-248.

50. Naber, R. C. G.; Mulder, M.; de Boer, B.; Blom, P. W. M.; de Leeuw, D. M. *Organic Electronics* **2006,** *7*, 132-136.

51. Naber, R. C. G.; Blom, P. W. M.; Gelinck, G. H.; Marsman, A. W.; de Leeuw, D. M. *Advanced Materials* **2005,** *17*, 2692-2695.

52. Gelinck, G. H.; Marsman, A. W.; Touwslager, F. J.; Setayesh, S.; de Leeuw, D. M.; Naber, R. C. G.; Blom, P. W. M. *Applied Physics Letters* **2005,** *87*, 092903.

53. Naber, R. C. G.; de Boer, B.; Blom, P. W. M.; de Leeuw, D. M. *Applied Physics Letters* **2005,** *87*, 203509.

54. Naber, R. C. G.; Massolt, J.; Spijkman, M.; Asadi, K.; Blom, P. W. M.; de Leeuw, D. M. *Applied Physics Letters* **2007,** *90*, 113509.

55. Lu, H.; George, T. A.; Wang, Y.; Ketsman, I.; Burton, J. D.; Bark, C.-W.; Ryu, S.; Kim, D. J.; Wang, J.; Binek, C.; Dowben, P. A.; Sokolov, A.; Eom, C.-B.; Tsymbal, E. Y.; Gruverman, A. *Applied Physics Letters* **2012,** *100*, 232904.

Chapter 5

Synthesis and Characterization of Mono and Few Layer $MoTe_2$ in the 2H, 1T' and 1T Phase

The following is taken from a manuscript to be submitted for publication. This collaborative work was performed by me and the following students and collaborators.

Thomas A. Empante, Yao Zhou[†], Velveth Klee, Ariana Nguyen, I-His Lu, Edwin Preciado, Michael Valentin, Ariana Naghibi Alvillar, Adam Berges, Miguel Isarraraz, Evan Reed[†], and Ludwig Bartels
Department of Chemistry and Material Science and Engineering Program, University of California – Riverside, Riverside, CA 92521 USA

[†]Department of Materials Science, Stanford University, Palo Alto, CA USA

Introduction

Transition metal dichalcogenides, TMDs, are of ongoing interest in the material science community because they offer a rich spectrum of physical properties in a well-defined material class. Prepared in the 2H phase with trigonal prismatic symmetry[1] around the Mo-cores, these molybdenum-based TMDs change from an indirect to a direct band gap semiconductor when thinned to the monolayer[2]. The latter lacks inversion symmetry giving rise to spin splitting at the K-point of the Brillouin zone.[3] A number of reports have shown that MoS_2 and $MoTe_2$ can also be prepared in the 1T' phase, in which one chalcogenide layer is offset with regards to the other so as to form an octahedral arrangement around the Mo-cores (1T-phase) and followed by a $_{2x}1$

reconstruction (1T'-phase). Like the 2H-phase, the 1T' phase lacks inversion symmetry and offers spin splitting, but - in contrast to the 2H-phase – it is metallic. There are numerous computational reports about the 1T phase of Mo-based TMDs yet experimental preparation of few-layer material has been elusive. Computational work predicts a metallic behavior of 1T:$MoTe_2$ but no spin-splitting because of the presence of an inversion center in the lattice.[4] Here we report on growth parameters that allow the preparation of all three phases of $MoTe_2$ and validation of their properties using a number of experimental and computational techniques.

Molybdenum-based TMDs consist of a hexagonal transitional metal layer sandwiched between two chalcogen layers (Fig. 23).[5] In the 2H phase, the chalcogen layers are in registry with the same hollow sites of the transition metal layer, whereas in the 1T phase the top and bottom chalcogen layer are in registry with different metal hollow sites.[6][7] 2H $MoTe_2$ is especially interesting as its band gap is in the near infrared just below that of silicon suggesting a range of Si-based photonic applications.[8][9][10] The ability to switch $MoTe_2$ between semiconducting and metallic properties suggests exploitation as a phase change material.[11][12] Yet while MoS_2 and, to a lesser degree, $MoSe_2$ and their $MoS_{2(1-x)}Se_{2x}$ alloys have been investigated intensively, $MoTe_2$ has found significant but less prolific experimental exploration largely because of its limited stability in air. From the perspective of a field of researchers accustomed to procedures developed for graphene, this is a severe shortcoming, yet it ought to be mentioned that the surface of $MoTe_2$ is no less oxidation resistant than that of bare silicon, the premier industrial semiconductor.[13] A number of schemes for the

passivation of $MoTe_2$ surfaces have been proposed. In this work we cover our films either with a layer of PMMA or by repeated deposition of approx. 1nm of aluminum followed by brief oxidation in air.

The overwhelming majority (but not all) prior publications on $MoTe_2$ have used exfoliated films often utilizing crystals grown by chemical vapor transport. Such films can be of very high quality and they lend themselves to a wide range of exploratory research, yet this procedure lacks a direct pathway to technological realization and produces films exclusively in the phase adopted by the original crystal.[14] A number of methods for post-exfoliation phase change have been described utilizing chemical and physical treatment of the film.[15] In this manuscript we utilize chemical vapor deposition, CVD, for the preparation of few-layer $MoTe_2$ films; CVD is a process well-established in semiconductor processing, compatible with current tool sets and eminently scalable. This offers a broad range of potential advantages toward future use of such films, especially if it is combined with spatial control over film growth.

Materials and Methods

CVD growth proceeds in a 12" long Lindberg clam shell type tube furnace with a tube diameter of 1 inch. The precursors used are molybdenum (VI) trioxide, MoO_3, and elemental tellurium powder (both from Aldrich) which are placed in 30mm x 8mm x 7mm alumina boats (from Coorstek). We utilize silicon wafer pieces as substrate and have obtained success not only on our standard substrates covered with 300 nm silicon

dioxide but also on bare silicon, lithium niobate, quartz, and sapphire substrates. The substrate is placed on the alumina boat carrying the MoO_3 powder. The boat containing the molybdenum oxide and the substrate is placed at the center of the furnace and the boat containing tellurium is placed 3.5" upstream of the flow from the center so that at the maximum process temperature the tellurium boat does not reach more than about 450°C. Prior to growth, the tube is purged with argon gas at 0.5 SCFH for 10 minutes; subsequently the flow is reduced to 0.01 SCFH until the end of the ramp up. The temperature ramp-up proceeds in two stages of 20 min each with the first stage raising the temperature from ambient to 500°C at a flow rate of 0.1 SCFH argon gas. The second stage raises the temperature to 650°C for $MoTe_2$ in the 2H phase and 680°C for targeting $MoTe_2$ in the 1T or 1T' phases. During a subsequent hold stage the temperature is maintained for 15 minutes while introducing hydrogen gas, H_2, at 0.05 SCFH and Ar at 0.05 SCFH.

Cooling of the CVD furnace proceeds in three steps: initially the furnace temperature is ramped down to 600°C in 10 minutes from the max temperature with equal flow rates of 0.05 SCFH H_2, CO_2, and Ar for a total flow rate of 1.5 SCFH. The second step ramps the furnace down from 600°C to 500°C in 20 min with a flow rate of 0.1 SCFH Ar. After the end of the second step the furnace power is turned off and the clam shell is allowed to cool naturally. The 2H phase is attained by leaving the clam shell closed until the furnace is under 100°C. The 1T' phase is attained by cooling to 350°C before the clam shell is opened. Finally, the 1T phase results if the clam shell is already

opened at 450°C. As soon as we open the clam shell the process tube is directly cooled by a fan at 250 SCFH flow rate.

Sample characterization utilizes a Horiba LabRam system with a 532nm laser for imaging and Raman spectroscopy, atomic force microscope (AFM) and probe station housed in a glove box utilizing a Keithley 2400 source meter and an SRS lock-in amplifier for DC and AC measurements, respectively.

Results

Fig. 24 shows Raman spectra and optical micrographs on the $MoTe_2$ films observed. We find the growth of $MoTe_2$ to nucleate in a circular fashion forming thick $MoTe_2$ film at the center that extends toward the periphery in a film of uniform few-layer thickness. The $MoTe_2$ film does not adopt straight edges, so that the edge shape does not indicate crystallographic quality or orientation. We attribute the absence of observable well-defined edges to the reorganization/mass transfer in the course of the phase transitions that the film undergoes during cooling. We expect the material to have a multitude of internal grain-boundaries/defects. Larger and well defined crystallite structures, as we produce molybdenum and tungsten disulfides and diselenides would be desirable, yet ongoing optimization of the growth process appears to be inherently limited by competition with phase relaxation toward 2H. The supporting information shows atomic force measurements of the layer thickness of our $MoTe_2$ samples.

Raman spectroscopy is used to identify and characterize the $MoTe_2$ phases. Samples not quenched during the growth process exhibit Raman peaks at 171cm^{-1} and 233cm^{-1}, as shown in panel a. These features agree well with peaks predicted from DFT calculations at 170cm^{-1} and 230cm^{-1}, at a deviation of 0.59% and 1.30%, respectively. Our values also agree well with results on exfoliated and CVD-grown 2H:$MoTe_2$.

Quenching at approx. 350C leads to a $MoTe_2$ film (panel b) that exhibits a number of Raman features that are typically associated with the 1T' phase of $MoTe_2$. Because of the expanded supercell and lower symmetry of this structure, the set of phonons is wider. In particular, we observe pronounced features at 80cm^{-1}, 85cm^{-1}, 102cm^{-1}, 112cm^{-1}, 126cm^{-1}, and 162cm^{-1} wavenumbers. These match our DFT predictions within an error of 1.25%, 4.49%, 2.00%, 0.90%, 1.61%, and 3.18%, respectively. The Raman modes observed in these films also correspond well to literature values on exfoliated and CVD films.

Quenching the film growth at 450C, we observe a Raman spectrum that is clearly distinct from the 1T' phase (panel c). It is significantly simpler consisting of two prominent modes only. Comparison to our computational work reveals good agreement of the two experimental Raman modes at 155cm^{-1} and 242cm^{-1} with the Raman modes of 1T:$MoTe_2$, which we predict at 159cm^{-1} and 240 cm^{-1} respectively. Based on this finding, we assign this phase to be 1T:$MoTe_2$. We are not aware of prior experimental observation of this phase.

Figure 25 compares the band structure of the three phases of $MoTe_2$: while 2H:$MoTe_2$ is a semiconductor, 1T' and also 1T are metallic phases. Notably, the 1T

phase has hexagonal symmetry; the presence of an inversion center prevents spin-splitting (in contrast to the 2H and 1T' phases).

We validate the assignment of the 1T phase by electrical transport measurements on all three phases. For contacts we utilize Ti/Au stacks fabricated using electron-beam lithography. Fig. 26 shows the results obtained for channel lengths of 0.5 microns. While 2H:$MoTe_2$ exhibits the properties of a semiconducting film including comparatively low conductivity, the 1T' and 1T both exhibit metallic behavior and very good conductivity.

The phases stability and transition temperatures[16] for each of the phases was calculated using DFT PBE. The 2H and 1T' phases utilized a primative hexagonal cell, whereass the 1T phases has a primative rectagular cell.

Fig. 25 shows the phase stability of the 2H, 1T', and 1T and the transition temperatures associated with the highest stability of each phase.

Post CVD and Raman characterization of the films, devices with scandium gold electrodes were fabricated using electron beam lithography. We report two-terminal electronic transport measurements for the three phases of $MoTe_2$ (2H, 1T, and 1T'). The measurements were performed at room temperature using a Keithley 2400. I-V characteristics indicate that the 1T phase is most conductive, followed by 1T' and then 2H.

Figures

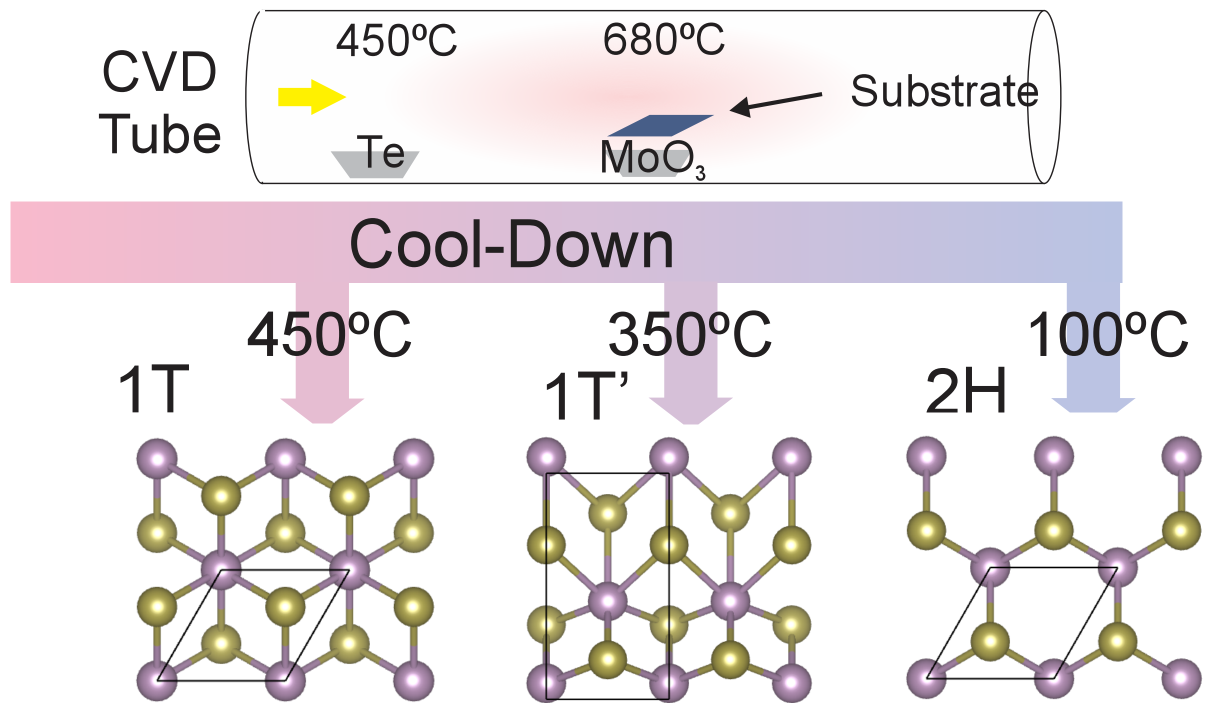

Figure 23. Overview of Preparative Technique: CVD growth of few-layer $MoTe_2$ proceeds in a tube furnace. The temperature at which the growth is quenched determines the resultant $MoTe_2$ phase.

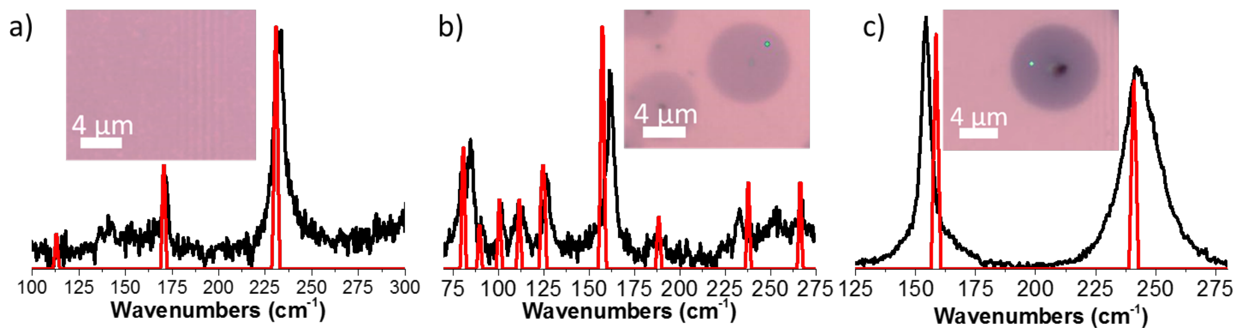

Figure 24. Shows comparison of the calculated (red) and experimental (black) Raman spectra for each phase of $MoTe_2$ a) 2H film, b) 1T' island, and c) 1T island.

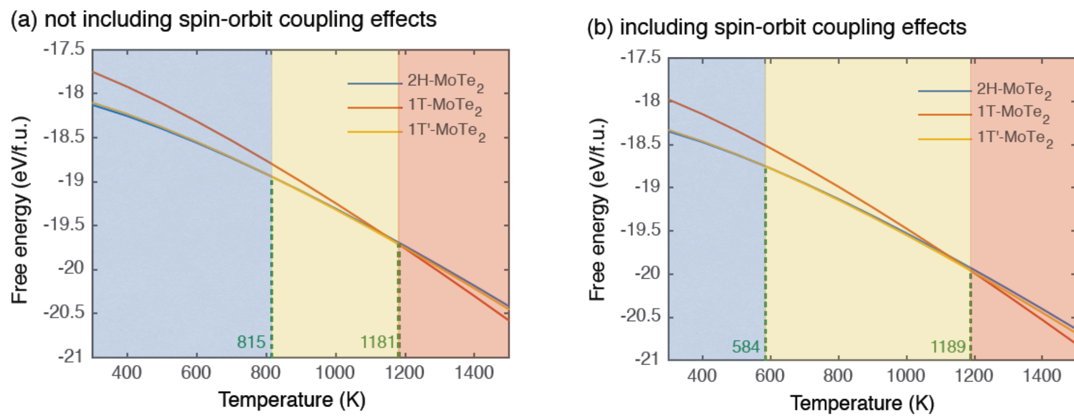

Figure 25. Shows the phase stability of the 2H, 1T’, and 1T and the transition temperatures associated with the highest stability of each phase.

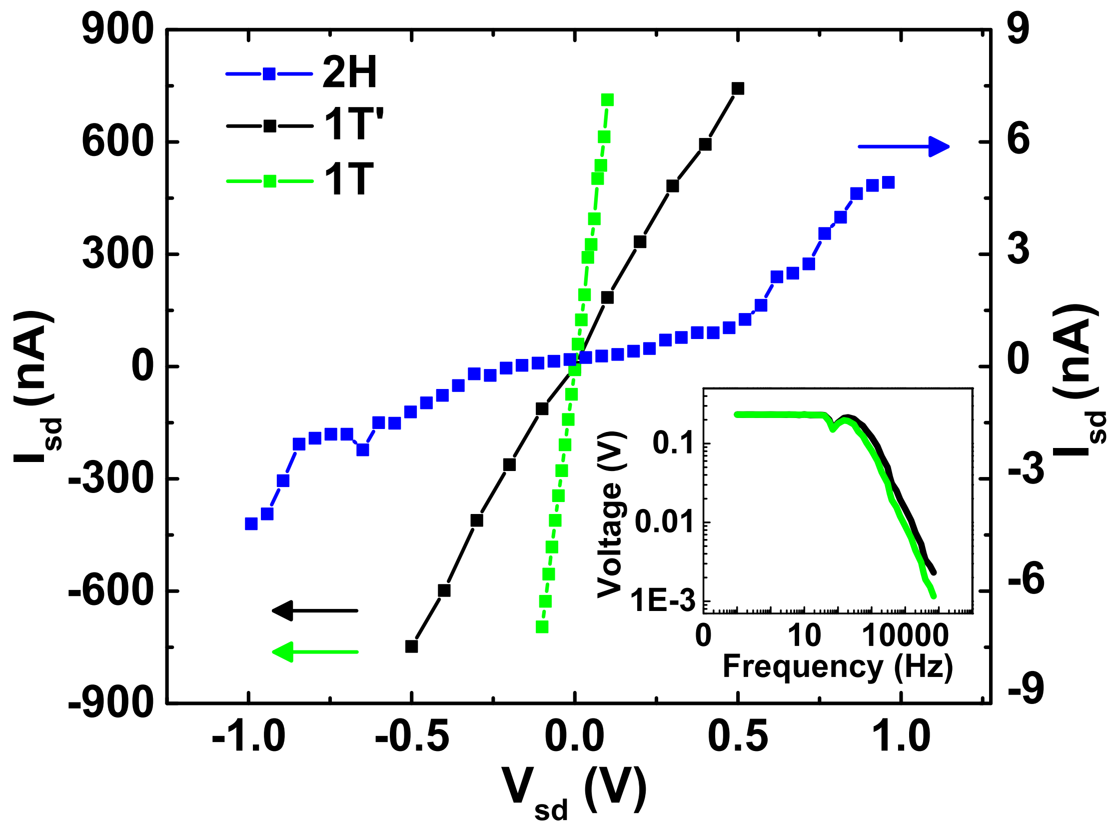

Figure 26. Shows the electronic transport of the 2H (blue), 1T' (black), and 1T (green) phases of $MoTe_2$. The inset shows the lock-in-amplifier data for $MoTe_2$ in the 1T (green) and 1T' (black).

References

1. Eda, G., Yamaguchi, H., Voiry, D., Fujita, T., Chen, M., Chhowalla, M., Photoluminescence from chemically exfoliated MoS_2. Nano letters 2011, 11 (12), 5111-5116.

2. Splendiani, A., Sun, L., Zhang, Y., Li, T., Kim, J., Chim, C.-Y., Galli, G., Wang, F., Emerging Photoluminescence in Monolayer MoS_2. Nano Letters 2010, 10 (4), 1271-1275.

3. Suzuki R., Sakano M., Zhang, Y. J., Akashi R., Morikawa D., Harasawa A., Yaji K., Kuroda K., Miyamoto K., Okuda T., Ishizaka K., Arita R., Iwasa Y., Valley-dependent spin polarization in bulk MoS_2 with broken inversion symmetry. Nat Nano 2014, 9 (8), 611-617.

4. Duerloo, K.-A. N., Li, Y., Reed, E. J., Structural phase transitions in two-dimensional Mo- and W-dichalcogenide monolayers. Nat Commun 2014, 5.

5. Radisavljevic B., Radenovic A., Brivio J., Giacometti V., Kis A., Single-layer MoS2 transistors. Nat Nano 2011, 6 (3), 147-150.

6. Keum, D. H., Cho, S., Kim, J. H., Choe, D.-H., Sung, H.-J., Kan, M., Kang, H., Hwang, J.-Y., Kim, S. W., Yang, H., Chang, K. J., Lee, Y. H., Bandgap opening in few-layered monoclinic $MoTe_2$. Nat Phys 2015, 11 (6), 482-486.

7. Hong, J., Hu, Z., Probert, M., Li, K., Lv, D., Yang, X., Gu, L., Mao, N., Feng, Q., Xie, L., Zhang, J., Wu, D., Zhang, Z., Jin, C., Ji, W., Zhang, X., Yuan, J., Zhang, Z., Exploring atomic defects in molybdenum disulphide monolayers. Nat Commun 2015, 6.

8. Ruppert, C., Aslan, O. B., Heinz, T. F., Optical Properties and Band Gap of Single- and Few-Layer $MoTe_2$ Crystals. Nano Letters 2014, 14 (11), 6231-6236.

9. Grant, A. J., Griffiths, T. M., Pitt, G. D., Yoffe, A. D., The electrical properties and the magnitude of the indirect gap in the semiconducting transition metal dichalcogenide layer crystals. Journal of Physics C: Solid State Physics 1975, 8 (1), L17.

10. Conan, A., Delaunay, D., Bonnet, A., Moustafa, A. G., Spiesser, M., Temperature dependence of the electrical conductivity and thermoelectric power in $MoTe_2$ single crystals. physica status solidi (b) 1979, 94 (1), 279-286.

11. Cho, S., Kim, S., Kim, J. H., Zhao, J., Seok, J., Keum, D. H., Baik, J., Choe, D.-H., Chang, K. J., Suenaga, K., Kim, S. W., Lee, Y. H., Yang, H., Phase patterning for ohmic homojunction contact in $MoTe_2$. Science 2015, 349 (6248), 625-628.

12. Song, S., Keum, D. H., Cho, S., Perello, D., Kim, Y., Lee, Y. H., Room Temperature Semiconductor–Metal Transition of $MoTe_2$ Thin Films Engineered by Strain. Nano Letters 2016, 16 (1), 188-193.

13. Liu, H., Han, N., Zhao, J., Atomistic insight into the oxidation of monolayer transition metal dichalcogenides: from structures to electronic properties. RSC Advances 2015, 5 (23), 17572-17581.

14. Böker, T., Severin, R., Müller, A., Janowitz, C., Manzke, R., Voß, D., Krüger, P., Mazur, A., Pollmann, J., Band structure of MoS_2, $MoSe_2$, and α-$MoTe_2$: Angle-resolved photoelectron spectroscopy and *ab initio* calculations. Physical Review B 2001, 64 (23), 235305.

15. Du, G., Guo, Z., Wang, S., Zeng, R., Chen, Z., Liu, H., Superior stability and high capacity of restacked molybdenum disulfide as anode material for lithium ion batteries. Chemical Communications 2010, 46 (7), 1106-1108.

16. Duerloo, K.-A. N., Reed, E. J., Structural Phase Transitions by Design in Monolayer Alloys. ACS Nano 2016, 10 (1), 289-297.